

AD-A077 871

VISIDYNE INC BURLINGTON MASS
BACKGROUND OPTICAL SUPPRESSION SYSTEM (BOSS), (U)
OCT 79 O SHEPHERD, T F ZEHNPFENNIG

F/6 20/6

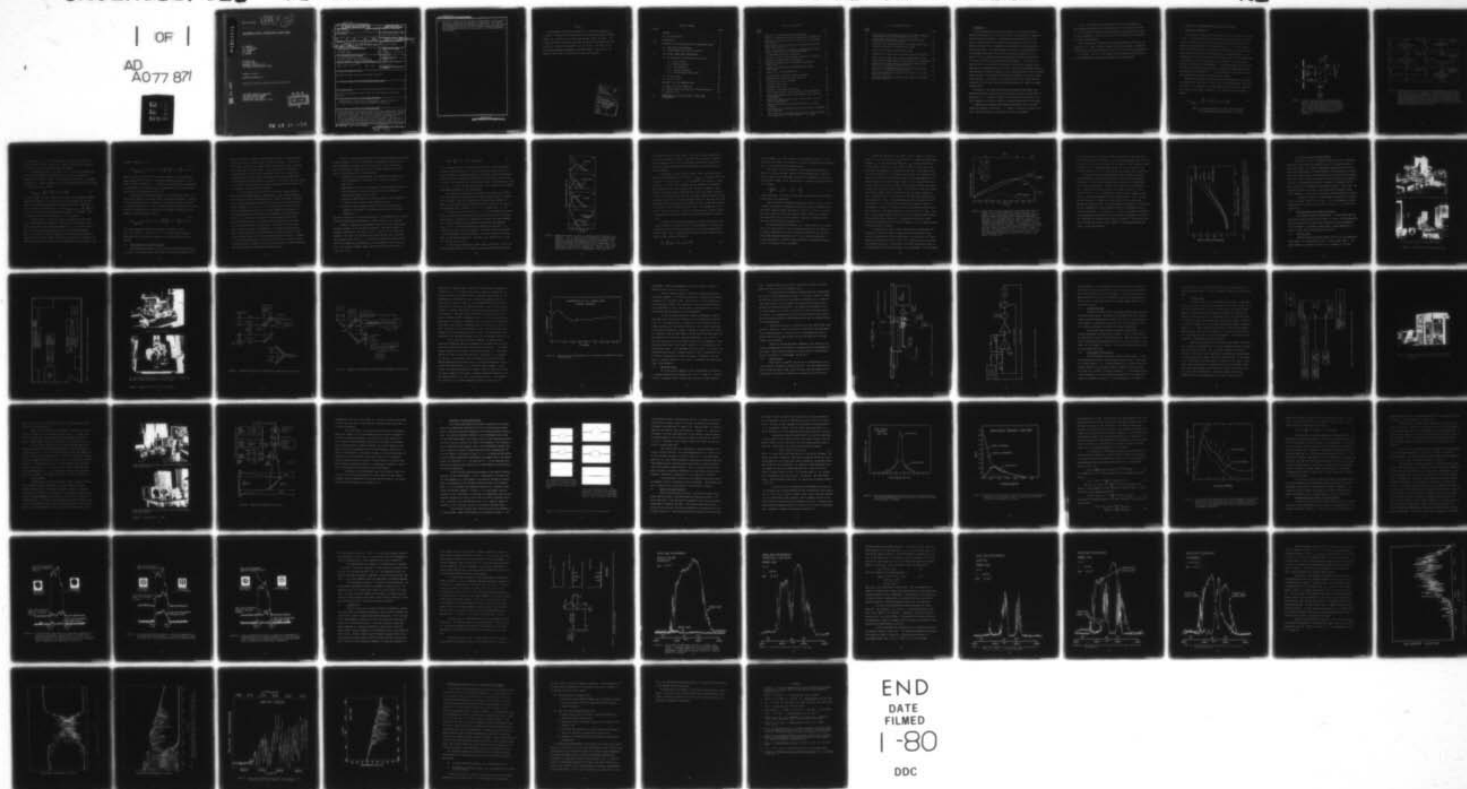
F19628-79-C-0005

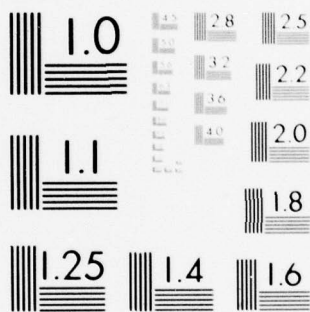
UNCLASSIFIED VI-493

AFGL-TR-79-0243

NL

| OF |
AD
A077 871





MICROCOPY RESOLUTION TEST CHART
NATIONAL BUREAU OF STANDARDS-1963-A

AD A 077871

AFGL-TR-79-0243

LEVEL II

12
B.S.

BACKGROUND OPTICAL SUPPRESSION SYSTEM (BOSS)

O. Shepherd
T.F. Zehnpfennig
S.A. Rappaport
W.P. Reidy
G. Vanasse

Visidyne, Inc.
19 Third Avenue
Northwest Industrial Park
Burlington, Massachusetts 01803

October 10, 1979

SCIENTIFIC REPORT NO. 2

Approved for public release; distribution unlimited

AIR FORCE GEOPHYSICS LABORATORY
AIR FORCE SYSTEMS COMMAND
UNITED STATES AIR FORCE
HANSCOM AFB, MASSACHUSETTS 01731

DDC
RECEIVED
DEC 11 1979
A

79 12 10 088

DDC FILE COPY

UNCLASSIFIED

SECURITY CLASSIFICATION OF THIS PAGE (When Data Entered)

(19) REPORT DOCUMENTATION PAGE		READ INSTRUCTIONS BEFORE COMPLETING FORM	
1. REPORT NUMBER (18) AFGL-TR-79-0243	2. GOVT ACCESSION NO.	3. RECIPIENT'S CATALOG NUMBER	
4. TITLE (and Subtitle) (6) BACKGROUND OPTICAL SUPPRESSION SYSTEM (BOSS)		5. TYPE OF REPORT & PERIOD COVERED Scientific Report No. 2 ✓	
6. AUTHOR(s) (10) O. Shepherd, T.E. Zehnpfennig, Saul Rappaport, W.P. Reidy of Visidyne, Inc.; Vanasse of AFGL		7. PERFORMING ORG. REPORT NUMBER (14) VI-493, SCIENTIFIC-2 8. CONTRACT OR GRANT NUMBER(s) (13) F19628-79-C-0005	
9. PERFORMING ORGANIZATION NAME AND ADDRESS Visidyne, Inc. ✓ 19 Third Avenue Burlington, Massachusetts 01703 390 862		10. PROGRAM ELEMENT, PROJECT, TASK AREA & WORK UNIT NUMBERS (16) 62101F 767010AD (17) 10	
11. CONTROLLING OFFICE NAME AND ADDRESS Air Force Geophysics Laboratory Hanscom Air Force Base, Massachusetts Contract Monitor: John A. Sandock/OPR		12. REPORT DATE October 10, 1979	
14. MONITORING AGENCY NAME & ADDRESS (if different from Controlling Office) (11) 1A Oct 79 (12) 77		13. NUMBER OF PAGES 76	
		15. SECURITY CLASS. (of this report) Unclassified	
		16. DECLASSIFICATION/DOWNGRADING SCHEDULE	
16. DISTRIBUTION STATEMENT (of this Report) Approved for public release; distribution unlimited.			
17. DISTRIBUTION STATEMENT (of the abstract entered in Block 20, if different from Report)			
18. SUPPLEMENTARY NOTES This work was supported in part by the Air Force Office of Scientific Research.			
19. KEY WORDS (Continue on reverse side if necessary and identify by block number) Interferometers, Double-Beam Interferometers, Spatial Filtering, IR Spectra, Fourier Spectroscopy, Background Suppression			
20. ABSTRACT (Continue on reverse side if necessary and identify by block number) A background optical suppression scheme utilizing a double-beam interferometer-spectrometer with coaligned beams and tailored modulation, transfer functions is presented. The system is designed to enhance the detectability of localized sources in the presence of strong spatially structured background in the IR region of the spectrum. The principles of the double-beam interferometer, several different schemes for tailoring the system MTF, and the results of calculations of the signal-to-			

DD FORM 1473

EDITION OF 1 NOV 65 IS OBSOLETE

UNCLASSIFIED

SECURITY CLASSIFICATION OF THIS PAGE (When Data Entered)

390 862

UNCLASSIFIED

SECURITY CLASSIFICATION OF THIS PAGE (When Data Entered)

20. noise for a variety of MTFs and types of backgrounds, are discussed. The optical, mechanical and electrical components of the Visidyne laboratory double-beam interferometer are described. The data system and laboratory test source are also discussed. Laboratory measurements demonstrating the spatial and spectral filtering capabilities are presented.

UNCLASSIFIED

SECURITY CLASSIFICATION OF THIS PAGE (When Data Entered)

PREFACE

We acknowledge the engineering support of G. Aurilio, R. Bucknam, and W. Sheehan in the design and construction of the Visidyne double-beam interferometer, and R. Wattson for assistance with the data system. We thank J. Rex of AFGL for helpful discussions concerning the design of the beamsplitter and mirror drive. We are also grateful to Dr. A.T. Stair, Jr. of AFGL for his continued encouragement and support of the BOSS project. This work was supported in part by the Air Force Office of Scientific Research.

Accession For	
NTIS GPO&I	
DDC TAB	
Unannounced	
Justification	
By	
Distribution/	
Availability Codes	
Dist	Avail and/or special
A	

TABLE OF CONTENTS

SECTION		PAGE
	FOREWARD	3
	LIST OF ILLUSTRATIONS	5
1.0	INTRODUCTION	7
2.0	PRINCIPLES OF THE BACKGROUND OPTICAL SUPPRESSION SCHEME. .	9
	2.1 Double-Beam Interferometers	9
	2.2 Tailored Modulation Transfer Functions	13
3.0	THE VISIDYNE DOUBLE-BEAM INTERFEROMETER	25
	3.1 The Double-Beam Interferometer Spectrometer	25
	3.1.1 Optical Design	25
	3.1.2 Mechanical Design	33
	3.1.3 Laser Reference	34
	3.1.4 Alignment Procedure.	37
	3.1.5 Interferometer Configuration	37
	3.2 The Data System	38
	3.3 The Test System	41
4.0	LABORATORY TESTS AND DEMONSTRATIONS	45
	4.1 Spatial Filtering Properties	47
	4.2 Combined Spatial and Spectral Filtering Properties. .	53
	4.3 Spectral Tests	58
5.0	CHARACTERISTICS AND APPLICATIONS OF DOUBLE-BEAM INTERFEROMETRY	73

LIST OF ILLUSTRATIONS

FIGURE NUMBER		PAGE
1	Schematic of ideal double-beam interferometer.	10
2	Schematic interferograms for ideal double-beam interferometer. .	11
3	Modulation transfer functions for several pairs of aberrated lens systems.	17
4	Sample signal-to-noise calculations for double-beam interfer- ometer with tailored MTF	21
5	Sample signal-to-noise calculations for double-beam interfer- ometers viewing variety of spatial backgrounds	23
6	Interferometer-spectrometer laboratory	26
7	Schematic layout of interferometer-spectrometer laboratory. .	27
8	Double-beam interferometer-spectrometer.	28
9a	Schematic of double-beam interferometer-spectrometer (upper level)	29
9b	Schematic of double-beam interferometer-spectrometer (lower level)	30
10	Transmission of CaF_2 beamsplitter	32
11	Interferometer mirror-drive mechanical diagram	35
12	Interferometer mirror-drive servo schematic	36
13	Laboratory data system schematic	39
14	Laboratory data system	40
15	Laboratory test system	42
16	Schematic of laboratory test system	43
17	Sample interferograms from the double-beam interferometer. . .	46
18	Point spread functions for the two beams of the laboratory interferometer.	49
19	Modulation transfer functions for the two beams of the lab- oratory interferometer.	50
20	Ratio of double-beam to single-beam response vs. spatial frequency	52
21	Double-beam and single-beam spectra of point source superposed on DC background.	55
22	Double-beam and single-beam spectra of point source superposed on a background with spatial frequency 1.1 cyc./deg.	56

LIST OF ILLUSTRATIONS (cont.)

FIGURE NUMBER		PAGE
23	Double-beam and single-beam spectra of point source superposed on a background with spatial frequency 7 cyc./deg.	57
24	Interferometer configuration for measuring absorption and transmission spectra of gas samples.	60
25	Double-beam and single-beam spectra of broadband light source. .	61
26	Single-beam transmission spectrum of NH_3 vapor	62
27	Double-beam absorption spectrum of NH_3 vapor	64
28	Superposition of double and single beam spectra of NH_3 vapor . .	65
29	Double-beam and single-beam spectra of polycarbonate filter . .	66
30	Double-beam absorption spectrum of NH_3 vapor (1 cm^{-1} resolution). .	68
31	Superposition of double-beam and single-beam spectra of NH_3 vapor (1 cm^{-1} resolution; near 4400 cm^{-1}).	69
32	Superposition of double-beam and single-beam spectra of NH_3 vapor (1 cm^{-1} resolution; near 5000 cm^{-1}).	70
33	Single-beam transmission spectrum of H_2O vapor (1 cm^{-1} resolution; near 3800 cm^{-1}).	71
34	Single-beam transmission spectrum of H_2O vapor (1 cm^{-1} resolution; near 5300 cm^{-1}).	72

1. INTRODUCTION

An optical background suppression technique is described which greatly enhances the detectability of localized sources in the presence of a nonuniform field of background radiation. The technique allows both the spatial and spectral characteristics of the source to be exploited in order to aid the detection process, while it suppresses the contribution of the background to the observed signal. The optical system consists of an imaging double-beam interferometer-spectrometer which has been configured to operate also as a spatial filter by suitably tailoring the modulation transfer functions (MTF) of the two main optical paths through the interferometer. In its role as a spatial filter, the double-beam interferometer preferentially suppresses the lower spatial frequencies found in the scene. The type of background suppression discussed here is especially important in the remote detection of small stationary sources against a strong spatially structured background in the infrared region of the spectrum. In particular, the technique minimizes the image processing required by significantly reducing the background before the image is recorded electronically.

The theory of the imaging double-beam interferometer-spectrometer with beams having suitably matched (tailored) modulation transfer functions (MTF) is presented in § 2. A number of systems with tailored MTFs are described, and their response to a variety of spatially structured backgrounds are calculated.

A laboratory double-beam interferometer-spectrometer with tailored MTF (defocussed system) is described in § 3. Details of the optical system, mirror drive, spectrum analyzer, and calibration facility are presented.

A series of laboratory tests and demonstrations with the double-beam interferometer-spectrometer have been carried out. These tests are discussed in § 4 and include the response of the interferometer-spectrometer to a range of spatial frequencies and the use of high resolution spectral discrimination in suppressing backgrounds.

Several applications of the optical background suppression technique are proposed in § 5. These include the remote sensing of pollutants in smokestack effluents, and the remote sensing of missile trails from surveillance satellites.

The various sections of this report have been prepared so that each may be read independently without detailed study of the other sections.

2. PRINCIPLES OF THE BACKGROUND OPTICAL SUPPRESSION SCHEME

2.1 Double-Beam Interferometers

The technique of double-beam interferometry was first suggested by Fellgett¹ in 1957. Subsequently, double-beam interferometers in various forms have been used for laboratory and astrophysical measurements in which the spectra to be measured were superimposed on large background signals²⁻⁷. In these measurements, essentially one input beam contained radiation from the source and background while the other input beam contained only background radiation. This has been done by using adjacent fields of view with a nearly uniform background, by simulating a well known background (e.g., blackbody), or by placing the source in one beam of the interferometer. In the present paper, we explore the efficiency of background suppression with a double-beam interferometer having coaligned beams and tailored MTFs. This new technique is compared to the background suppression achieved by offsetting the two beams.

Consider the following idealized double-beam interferometer with a dielectric beamsplitter illustrated in Figure 1, and its possible outputs illustrated in Figure 2. For radiation with a broad spectral distribution $B(\sigma)$, entering at A_1 (beam 1), the output of detector D_1 as a function of path difference x is given by:

$$D_1(x)_{\text{(beam 1)}} = \int_{\sigma_1}^{\sigma_2} B_1(\sigma) \left[\frac{1}{2} + \frac{1}{2} \cos 2\pi\sigma x \right] d\sigma. \quad (1)$$

where σ is the wave number and σ_1 and σ_2 are the spectral limits imposed by the system detector or a filter.

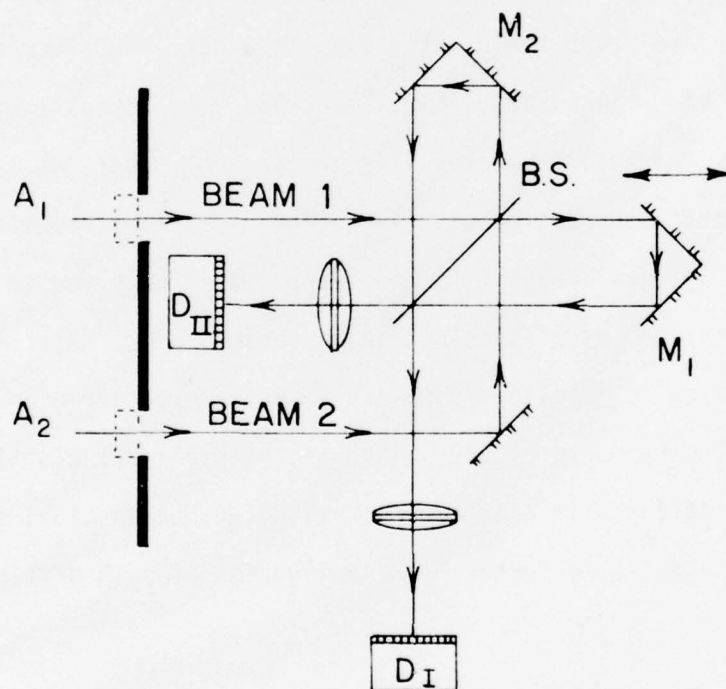


FIGURE 1: Schematic of double-beam interferometer with a tailored modulation transfer function (MTF). Beams of radiation entering the two arms of the interferometer pass through optical components at A_1 and A_2 which define the MTFs for the two arms. Mirrors M_1 and M_2 are roof-type retro-reflectors. The ¹dielectric beamsplitter is labelled B.S..

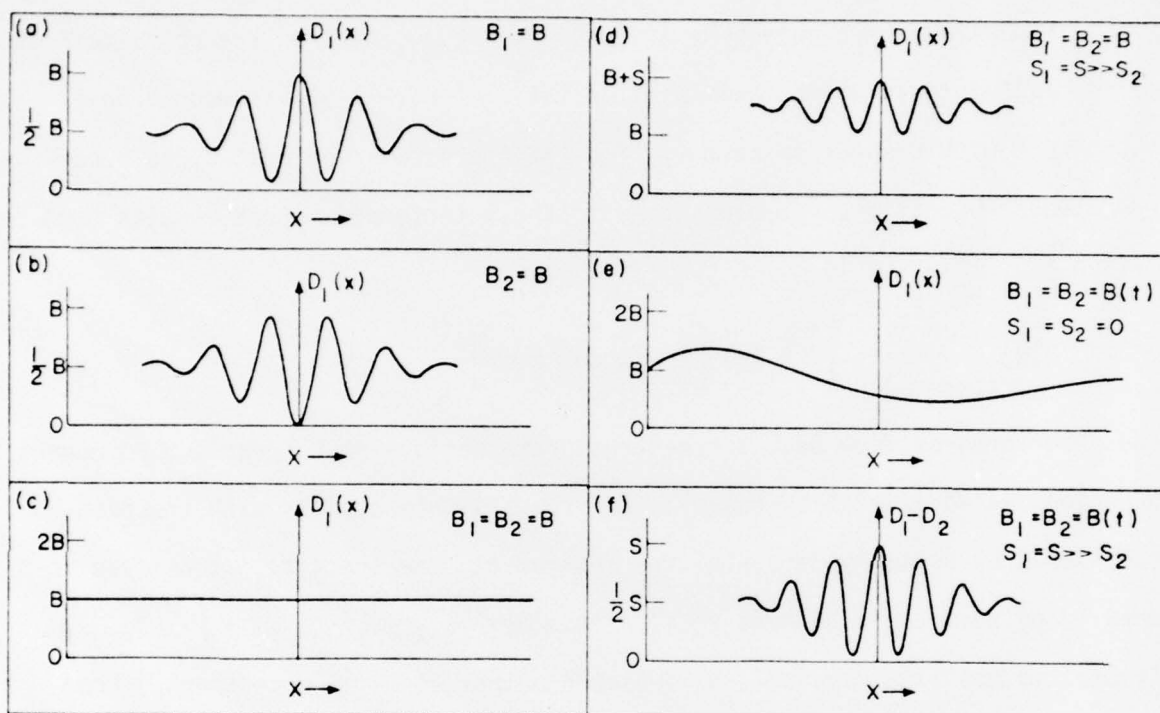


FIGURE 2: Schematic interferograms for a dual-beam interferometer, recorded by a single detector (D_1). a) radiation of integrated intensity B entering arm 1 only; b) radiation entering arm 2 only; c) equal fluxes of background radiation entering both arms; d) equal background fluxes and a highly unbalanced source flux in the two arms; e) an equal but time-varying background flux entering both arms; and f) difference in interferograms from detectors D_1 and D_2 with equal but time varying background fluxes and unbalanced point source fluxes.

The interferogram, D_1 , will look qualitatively like the curve in Figure 2a; for illustrative purposes, we have used a spectral distribution $B(\sigma)$ which is Gaussian in shape and centered on a non-zero frequency.

Radiation which enters at A_2 (beam 2, Fig. 1) strikes the opposite face of the main interferometer beamsplitter (at 0). Beam 2 is assumed to be incoherent with respect to beam 1. The interferogram from beam 2, as recorded by detector D_1 , is then complementary to the interferogram that results from beam 1 (see Fig. 2b), and is given by:

$$D_1(x)_{\text{(beam 2)}} = \int_{\sigma_1}^{\sigma_2} B_1(\sigma) \left[\frac{1}{2} - \frac{1}{2} \cos 2\pi\sigma x \right] d\sigma. \quad (2)$$

The interferogram from beam 2 takes this form because each frequency component undergoes an additional π - phase shift from its interactions with the beamsplitter. By suitably designing the instrument, the spectral intensities in beam 1 and beam 2 can be made equal. Then $D_1(x)_{\text{(beams 1 and 2)}} = \int_{\sigma_1}^{\sigma_2} \frac{B(\sigma)}{2} d\sigma$. If $B(\sigma)$ is not time varying, the detector output at D_1 is a constant. From the symmetry of the figure, the output of D_2 is also constant.

Consider now the case where the signals introduced into the two arms of the interferometer are unbalanced. Specifically, let the signals from a point source in the field of view be unbalanced (i.e., $S_1(\sigma)$ in arm 1 and $S_2(\sigma)$ in arm 2), while the background levels are still quite closely balanced ($B_1(\sigma) = B_2(\sigma) = B(\sigma)/2$). Several techniques are available for producing the imbalance in source signals (while leaving the background levels balanced), and these will be discussed in Section 2.2. The imbalance in target signals will be

recorded in detector D_1 as:

$$D_1(x) = B + \frac{1}{2} (S_1 + S_2) + \frac{1}{2} \int_{\sigma_1}^{\sigma_2} [S_1(\sigma) - S_2(\sigma)] \cos 2\pi\sigma x \, d\sigma. \quad (3)$$

(beams 1&2)

where $B = \int B(\sigma) d\sigma$ and S_1 and S_2 are similarly defined. This interferogram is shown schematically in Figure 2d. The observed modulation amplitude is equivalent to signal of intensity $S_1 - S_2$ entering only one arm of the interferometer. This modulating signal from the source is superposed on the DC level provided by the source plus background (see Fig. 2d).

The preceding assumes the background is not fluctuating with time. It is also possible, however, to suppress temporal background fluctuations. Although such fluctuations would occur in both beams, they would be in phase and result in a spurious modulation in D_1 (Fig. 2e), which reduces the sensitivity for source detection. We note that this limitation can be overcome by making use of the symmetry of the interferometer (Fig. 1):

$$D_2(x) = B + \frac{1}{2} (S_1 + S_2) + \frac{1}{2} \int_{\sigma_1}^{\sigma_2} [S_2(\sigma) - S_1(\sigma)] \cos 2\pi\sigma x \, d\sigma. \quad (4)$$

(beams 1&2)

If we now electronically subtract the outputs of detectors D_1 and D_2 :

$D_1(x) - D_2(x) = \int [S_1(\sigma) - S_2(\sigma)] \cos 2\pi\sigma x \, d\sigma$. The contribution from equal background fluxes in the two arms cancels, while the source modulations are additive.

2.2 Tailored Modulation Transfer Functions

The background suppression in the interferogram represented by equation 3 is based on the assumption that one can obtain a significant imbalance in the

source signal with no imbalance in the background signal. As a simple example, consider a point source viewed against a uniform background. If the optical axes of beam 1 and beam 2 are slightly offset, then the two images of the beams will be displaced in the image plane. For an appropriately sized detector no suppression of the point source interferograms will occur. However, displacement does not affect a uniform background and the modulation amplitude in the background interferogram will be suppressed. The problem with this scheme is, of course, that the background may not be uniform from point to point, and its suppression will therefore be incomplete.

In a first attempt to find a more efficient means of background suppression, we considered deliberate introduction of a small amount of defocus into one of two coaligned interferometer arms. Images from either of the arms can be slightly defocussed on the detector face by placing a weak positive or negative element at A_1 or A_2 (Fig. 1). This has the overall effect of suppressing the modulation amplitude for the more smoothly varying regions of the background, while not suppressing the modulations of point-like sources (see Eq. 3). Intuitively, this effect can be understood by noting that a slightly defocussed image of a smoothly varying background does not differ much from the corresponding in-focus image. Thus, when the in-focus background image from one beam is superimposed in coincidence on the defocused image from the other beam, the interferogram is reduced to nearly a DC level on each detector element, and effective background suppression occurs. However, a slightly defocussed image of a point-like source differs strongly from the corresponding in-focus image; thus, the source interferogram is highly modulated when the two images are superposed on the detector face.

Defocusing is the only one of many possible methods for altering the response of optical systems of this type; the two MTFs corresponding to the two arms of the interferometer can readily be tailored to satisfy various system requirements. In addition to defocusing, some of the other techniques which can be used in altering MTF pairs are listed as follows:

1. Introduction of controlled amounts of an aberration or some special optical component into the system (e.g., spherical aberration, a weak axicon).
2. Adjustment of the ratio of the diameters of the two entrance apertures.
3. Phase apodization of an entrance aperture by the introduction of phase-shifting annular rings or disks.
4. Transmission apodization of an entrance aperture by the introduction of annular rings or disks of neutral density filters.
5. Controlled, small amplitude mechanical oscillation of an optical component in the system at a frequency high compared to the system response time.

The above techniques can be applied individually or in combination to one or both arms of the double-beam interferometer to produce changes in the system MTF.

Consider a double-beam interferometer comprised of two arms each having different responses to various spatial frequencies. When the two beams are combined at the detector, the effect is that of a spatial filter that ideally responds to the signal from the point source being studied, while suppressing the background signal (see Eq. 3). The effective modulation transfer function (MTF) of the double-beam interferometer is the difference in MTFs of the two arms. For circularly symmetric beams, the effective MTF can be written as (see e.g., ref. 9):

$$\text{MTF}(K) \propto \int_0^{\infty} [I_1^2(R) - I_2^2(R)] J_0(2\pi RK) R dR \quad (5)$$

In this expression, $I^2(R)$ is the diffraction pattern as a function of radial distance in the image plane, J_0 is a zero order Bessel function, and K is a spatial frequency. We emphasize that the "subtraction" process discussed here refers only to the modulation amplitude in the interferogram, and not to the DC signals. We assume here that the wavelength range is sufficiently restricted (i.e., $\Delta\lambda/\lambda \lesssim 0.1$) that the MTF may be assumed to be a constant for all spectral wavelengths contributing to the interferogram.

For purposes of illustration, we consider here tailored pairs of MTFs that result when one of the following four types of aberrations is introduced into the system. These will be specified by the aberration function $\delta(\rho)$, where ρ is the distance from the center of the pupil in units of its radius a . The aberrations are: 1) defocus [$\delta(\rho) = C\rho^2$]; 2) π -phase shift [$\delta = \pi$ for $\rho < \rho_0$]; 3) linear aberration (axicon) [$\delta(\rho) = C\rho$]; and 4) "wobbled lens" system. Figure 3 illustrates the tailoring of pairs of MTFs in the ways listed above, with the goal of suppressing, as completely as possible, the system response to all spatial frequencies below about one-fourth the cutoff frequency ($K_{\max} = 2a/\lambda$). The MTFs were numerically computed from equation 5. In Figures 3a, b, and c the curve labelled "A" represents the MTF for the path of the interferometer with no aberrations. The curves labelled "B" are the MTFs for the specified aberration. The heavy curve, labelled "A-B", is the effective MTF of the system.

At low spatial frequencies, the MTFs shown in Figures 3a, b, and c are characterized by $\text{MTF}(K=0) = 0$ followed by an approximately linear rise with

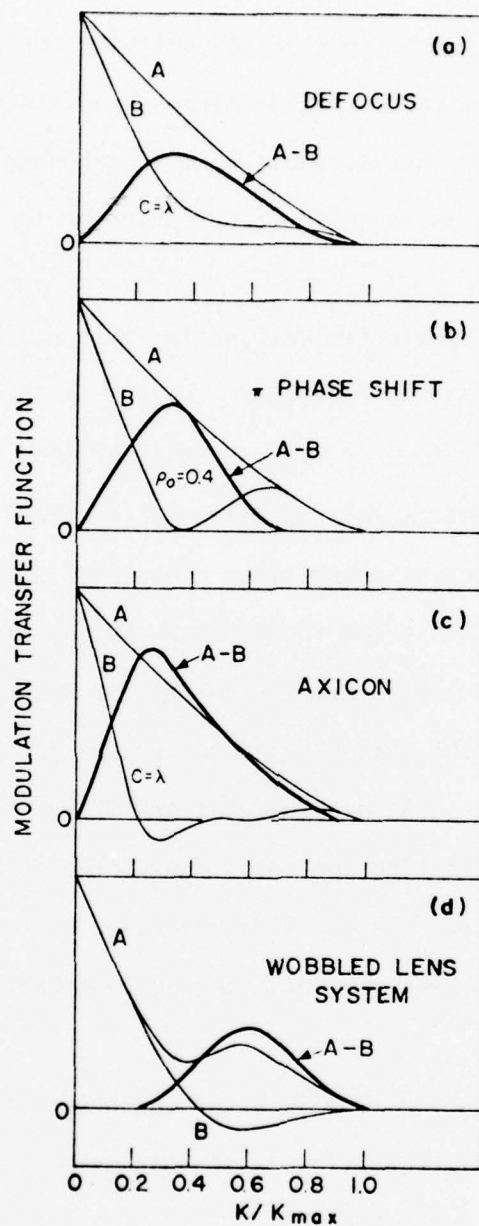


FIGURE 3: Modulation transfer functions for several pairs of aberrated lens systems. In a), b), and c) the curve labelled A is the MTF for an ideal lens. The curve labelled B is the MTF corresponding to the aberration which has been introduced into one of the arms. The curve A-B represents the effective MTF of the interferometer. The "wobbled lens" system in d) is described in the text. K_{\max} is the diffraction limited cut-off frequency, $2a/\lambda$, where a is the aperture (beam) radius and λ is the wavelength of the radiation.

K. Note that for these 3 cases there is no spatial frequency, other than $K=0$, which is perfectly filtered. Of the MTFs shown in Figure 3, defocus is the most convenient for use in the double-beam interferometer because the MTF may be changed without the need for fabrication or installation of new optical components.

As an example of a more efficient spatial filter, we have devised at least one system with $MTF(K) = 0$ for all $K \leq 0.2K_{\max}$. This system consists of a lens with a π -phase shift for $\rho < 0.3$, and another lens that has a π -phase shift for $\rho < 0.98$, and that is rotated off-axis (wobbled) at a frequency rapid compared to the system response time. The lens is wobbled in such a manner as to cause the point spread function in the image plane to rotate in a circle at a constant angular velocity. The angular diameter of this circular motion was set at $3\lambda/8a$. The chosen parameter values for the phase shifts and the angular extent of the wobble are somewhat arbitrary in that other combinations can also yield an effective spatial filter. The computed MTF for this system is shown in Figure 3d. The only disadvantage of this system is that it is somewhat more difficult to implement than those summarized in Figures 3a, b, and c.

The signal $S(\vec{R})$ recorded by a detector in the focal plane array, from a source located at a position \vec{R} relative to that detector, is given by the convolution of the system point spread function, the source shape and the detector shape. This is equivalent to the inverse Fourier transform of the product of the respective transforms.:

$$S(\vec{R}) \propto \int \tau_{\text{opt}}(\vec{K}) \tau_s(\vec{K}) \tau_d(\vec{K}) e^{i\vec{K} \cdot \vec{R}} d\vec{K} \quad (6)$$

In this integral τ_{opt} is the effective MTF of the optical system, τ_s is the transform of the spatial distribution of the source as projected on the detector, and τ_d is the transform of the detector shape.

The response of the interferometer to the background radiation will depend critically on the power spectrum of the background spatial structure. The rms signal from the background (noise) that is recorded by a given focal plane detector element, as the interferometer is pointed in various directions, is (cf. Fried)¹⁰:

$$N \propto \left[\int \beta(\vec{K}) |\tau_{\text{opt}}(\vec{K})|^2 |\tau_d(\vec{K})|^2 d\vec{K} \right]^{1/2} \quad (7)$$

In this expression, $\beta(\vec{K})$ is the two dimensional power spectrum of the spatial distribution of the background.

Ideally, the MTF is designed to optimize the signal to noise. In most situations of interest, the background spectrum has strong contributions from low spatial frequencies while the source of interest is close to, or smaller than, the diffraction limit of the optical system. We have thus attempted to construct MTFs with a minimum response to low spatial frequencies while maximizing the high frequency response (Fig. 3).

We have evaluated the performance (i.e., signal-to-noise) of a variety of MTFs for several general classes of background structure. We discuss, as an example, backgrounds with spatial structure characterized by a two dimensional power spectrum proportional to K^{-n} . It can easily be shown that a uniform background or a linearly varying background is completely eliminated by any of the spatial filters considered.

Consider two idealized classes of MTF; these are shown as an inset to Figure 4. The first (Type I) has $\tau_{\text{opt}}(K)=0$ for all K below some cutoff spatial frequency K_0 . In the second filter (Type II), τ_{opt} increases linearly from $K=0$ (with slope α) until its value is equal to that of an ideal lens, from which point (also denoted K_0) it matches the ideal lens. When computing the rms noise from equation (7), one generally must assume a low frequency cutoff (usually set by the size of the field of view) since a background with a K^{-n} spectrum does not have a well defined variance. In our calculations we have assumed a field of view equal to 1000×1000 resolution elements; the results are relatively insensitive to this choice. For simplicity in the calculations we have also assumed circularly shaped pixels with an angular diameter of $\lambda/2a$. The signal-to-noise ratios for both of the above idealized MTFs have been computed for a range of background power spectra; the results for a K^{-2} spectrum (see, e.g., ref. 10 and 11) are shown as an example in Figure 4. The ordinate is the ratio of signal-to-noise of the specified system to that for an ideal lens. The optimum cutoff for a Type I filter is $\sim 0.7K_{\text{max}}$. The Type II filter becomes highly effective as $K_0 \rightarrow 1$ even though its peak response to point sources becomes very small. For comparison, the signal-to-noise ratios for the "wobbled lens" (Fig. 3d) and "defocus" (Fig. 3a) spatial filters are also indicated in Figure 4.

As a comparison to spatial filters which utilize coaligned beams and tailored MTFs, we have repeated the signal-to-noise calculations for the case of an interferometer with two offset beams. The results for a K^{-2} background power spectrum are shown in Figure 4 as a function of the offset angle. The background suppression is optimized for an offset approximately equal to the diffraction limited angular resolution of the instrument. For large offsets,

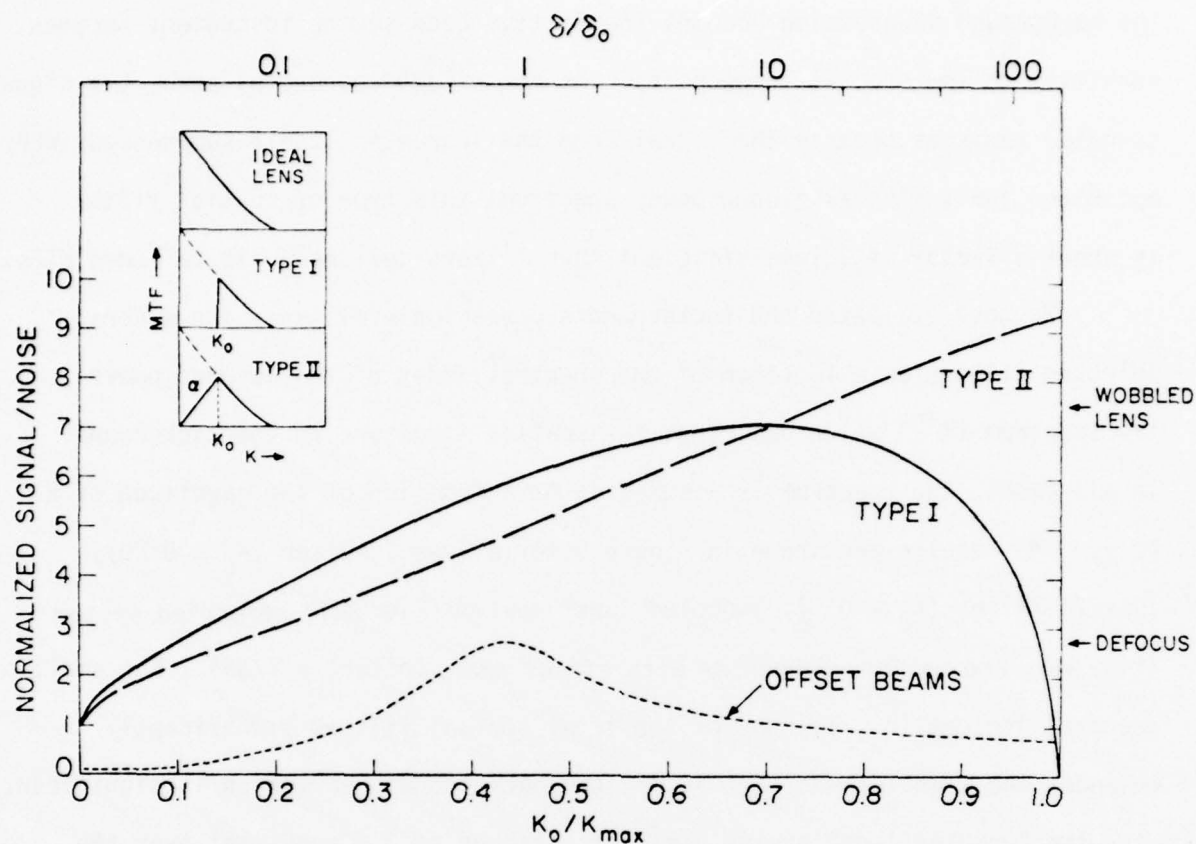


FIGURE 4: Sample signal-to-noise calculations for a double-beam interferometer, with a tailored modulation transfer function. The example is for a point-source viewed against a background whose spatial components are described by a two-dimensional power spectrum $\propto K^{-2}$. For idealized Type I and Type II spatial filters (see text), the calculated signal-to-noise is plotted vs. the parameter K_0 (defined in the inset). The limiting case of $K_0 \rightarrow 0$ represents an unfiltered lens system. For comparison, the signal-to-noise calculations for a double-beam interferometer with offset beams are shown as a function of the off-set angle δ (upper abscissa; δ is expressed in units of $\delta_0 = \lambda/2a$). The signal-to-noise for the special case of a "wobbled lens" system (Fig. 3d) and a "defocused" system (Fig. 3a) are also indicated on the figure for comparison.

the background suppression becomes ineffective because the instrument becomes sensitive to low spatial frequencies. As the offset approaches zero, the signal-to-noise vanishes because the signal from the source is itself suppressed. When optimized for a K^{-2} background power spectrum, this type of spatial filter is about a factor of 3 less efficient than filters designed with tailored MTFs.

We have evaluated the background suppression efficiency for several selected filters as a function of the spectral index of the assumed power-law spectrum (K^{-n}) which describes the spatial structure in the background. In all cases, the spectrum is assumed to be a function of the magnitude of K only. The results are shown in Figure 5 for a Type I filter ($K_0 = 0.20$), Type II filter ($K_0 = 0.5$), "wobbled lens" system (Fig. 3d), defocused system (Fig. 3a), and an interferometer with offset beams (offset $\approx \lambda/2a$). For small spectral indices ($n \lesssim 1$) none of the trial spatial filters significantly enhances the signal-to-noise. At $n=2$ the background suppression is significant, with the "wobbled lens" system yielding a factor of 3 improvement over the offset pointing mode. As n increases ($n \gtrsim 4$) there are substantial differences in performance among the filters of up to two orders of magnitude. The filters with effectively no response below $\sim 0.2K_{\max}$ are superior. The offset pointing mode, which does not provide a good "average" of the background around the source, is the least effective.

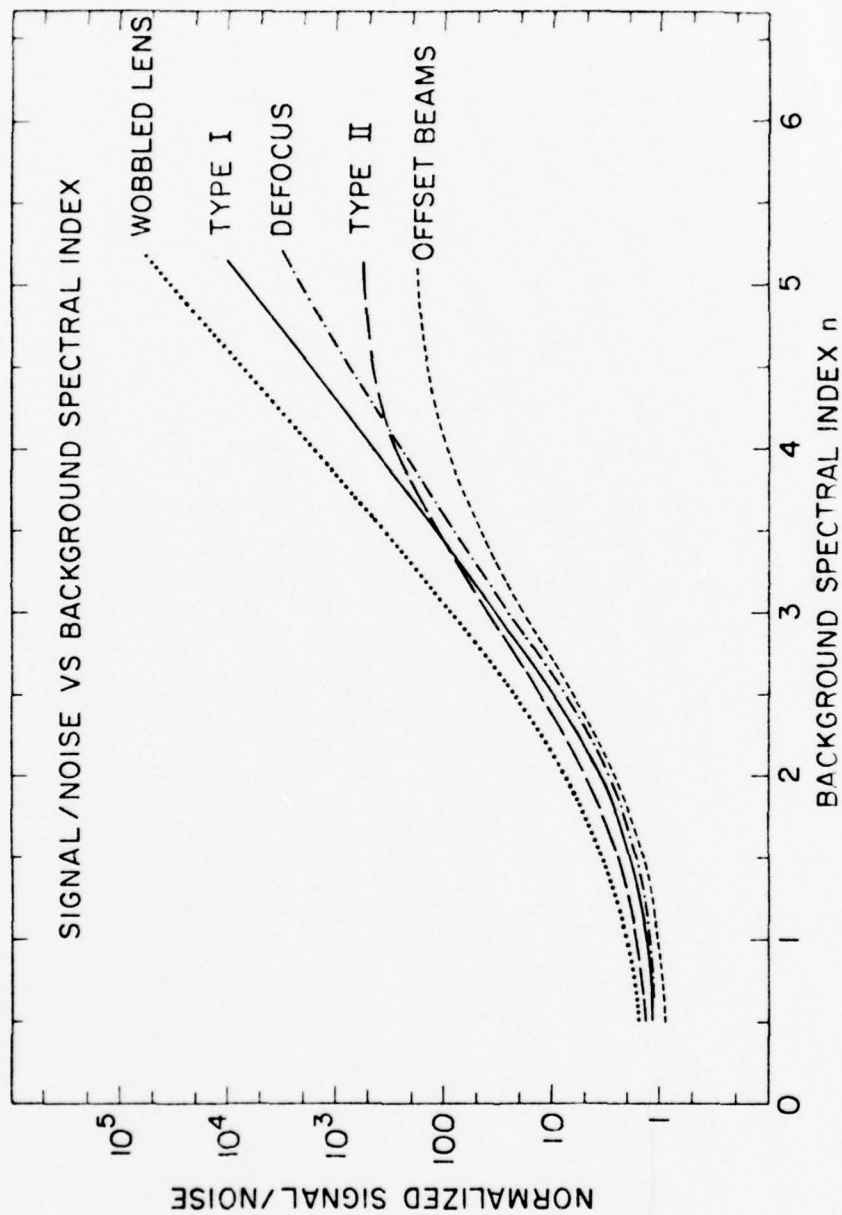


FIGURE 5: Signal-to-noise calculations for double-beam interferometers with a variety of spatial filters vs. the index of the power-law spectrum which describes the spatial structure in the background. The source is assumed to be point-like. Type I and Type II spatial filters are described in Figure 4.

3. THE VISIDYNE DOUBLE-BEAM INTERFEROMETER

During the past year, Visidyne has designed and built a laboratory double-beam interferometer-spectrometer for use in its background optical suppression scheme. The working interferometer system presently features a double-beam interferometer (2-cm beam aperture), tailored modulation transfer function for the two beams, servo-controlled drive for the moving retroreflecting mirror, laser retardation reference system, PbS detector and associated electronics, 16K hardwired fast Fourier transform (FFT) analyzer, and CRT plus X-Y plotter for displaying interferograms and spectra in real time. The laboratory facility also includes a test setup that can simulate a point source immersed in a controllable sinusoidally varying background at infinity.

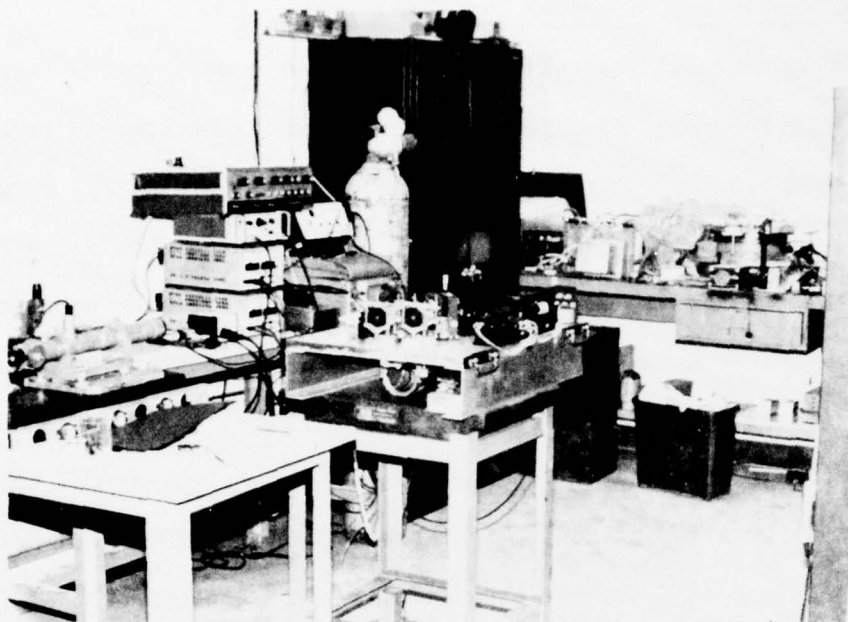
The general layout of the interferometer laboratory is pictured in Figure 6 and shown schematically in Figure 7. The interferometer, the data system and the test facility are described in detail in § 3.1, 3.2 and 3.3, respectively.

3.1 The Double-Beam Interferometer-Spectrometer

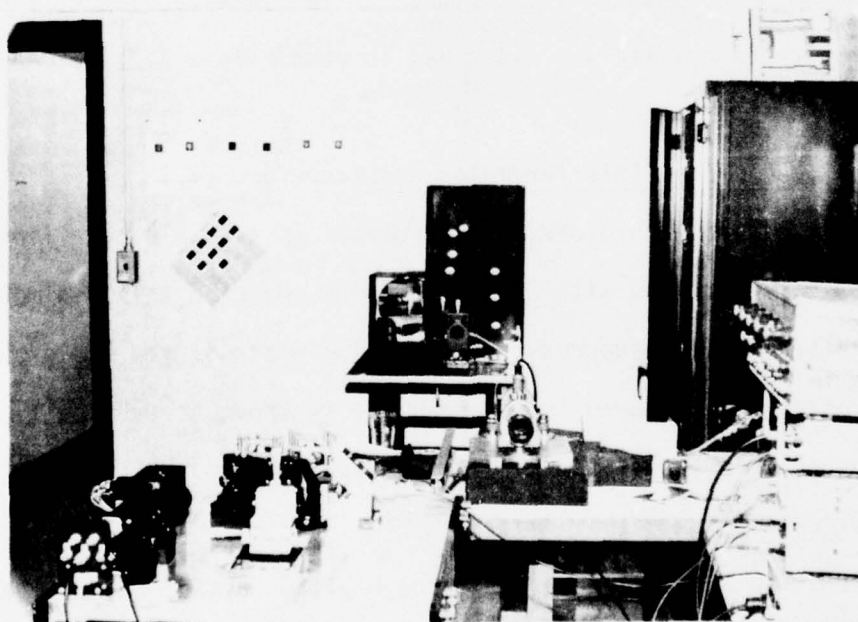
The Visidyne laboratory interferometer is a double-beam input and dual-detector output design with CaF_2 lenses to provide a tailored modulation transfer function for the suppression of spatially structured background. The interferometer is pictured in Figure 8 and is shown schematically in Figure 9a (upper level) and Figure 9b (lower level).

3.1.1 Optical Design

Radiation enters the system through either a flat CaF_2 compensator plate (beam 1) or a defocusing CaF_2 lens (1 m focal length; beam 2). The beam diameters are separately variable up to a diameter of 2 cm using



Interferometer, mounted on Al tooling plate and optical bench.



Test source as seen from the interferometer.

FIGURE 6: Interferometer-spectrometer laboratory.

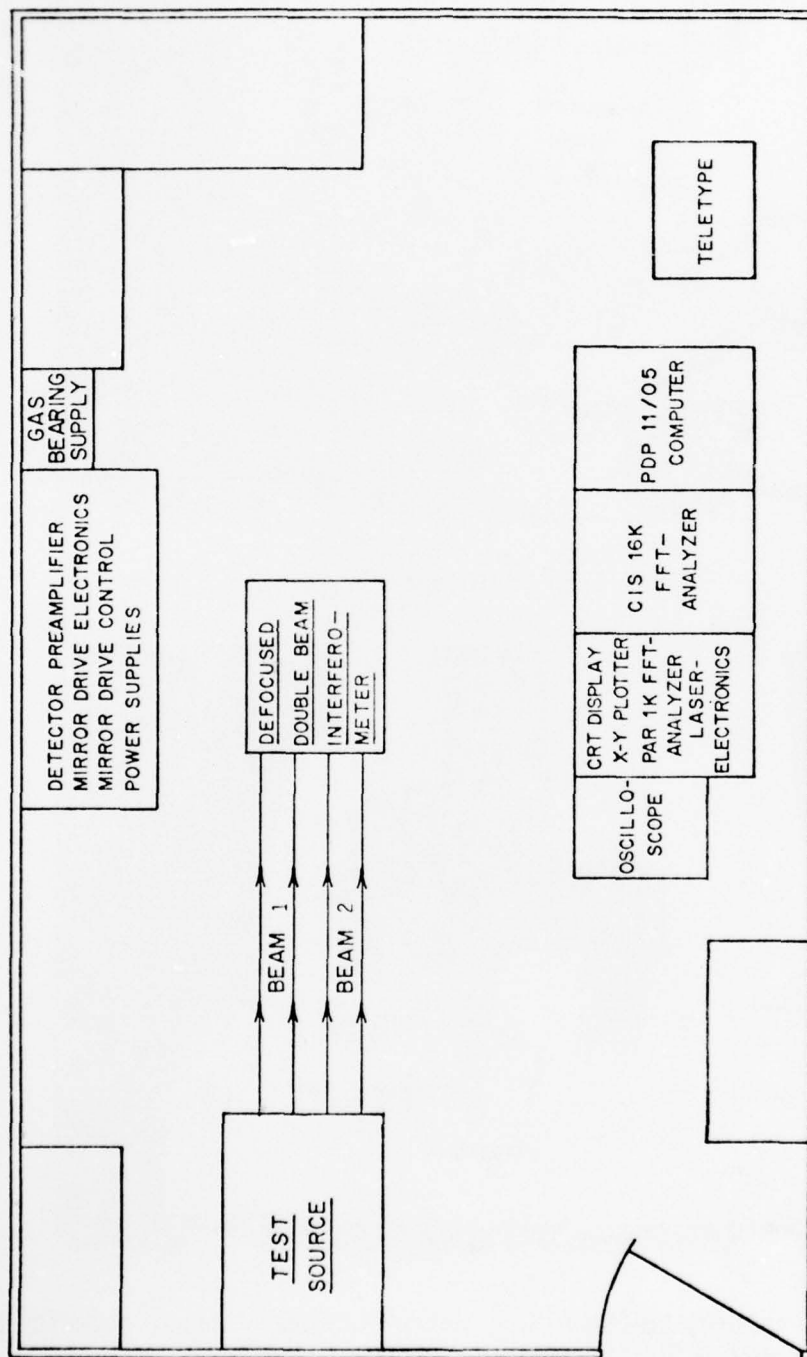
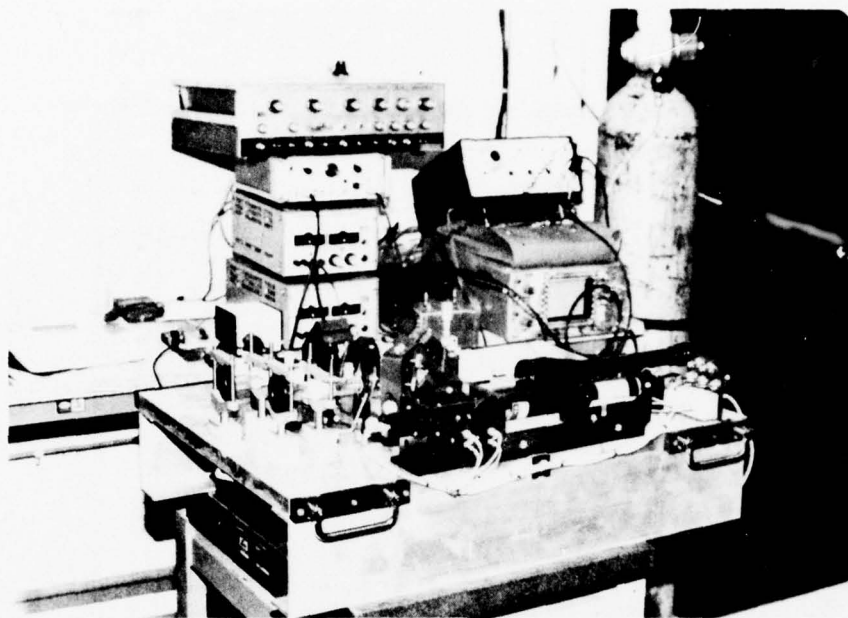
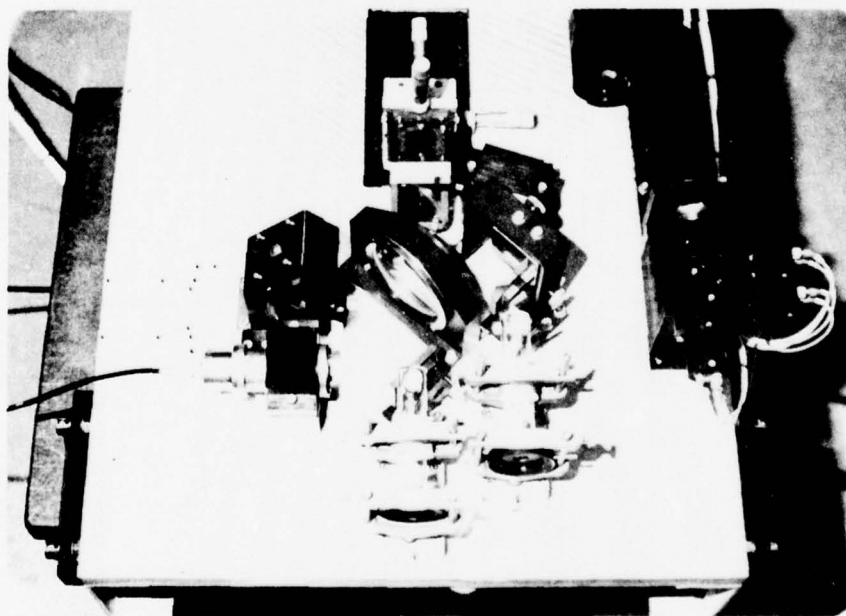


FIGURE 7: Schematic layout of interferometer - spectrometer laboratory.



Side view of interferometer.



Top view, showing beamsplitter, retroreflecting mirrors, detector II, gas cells, and laser retardation reference system.

FIGURE 8: Double-beam interferometer-spectrometer.

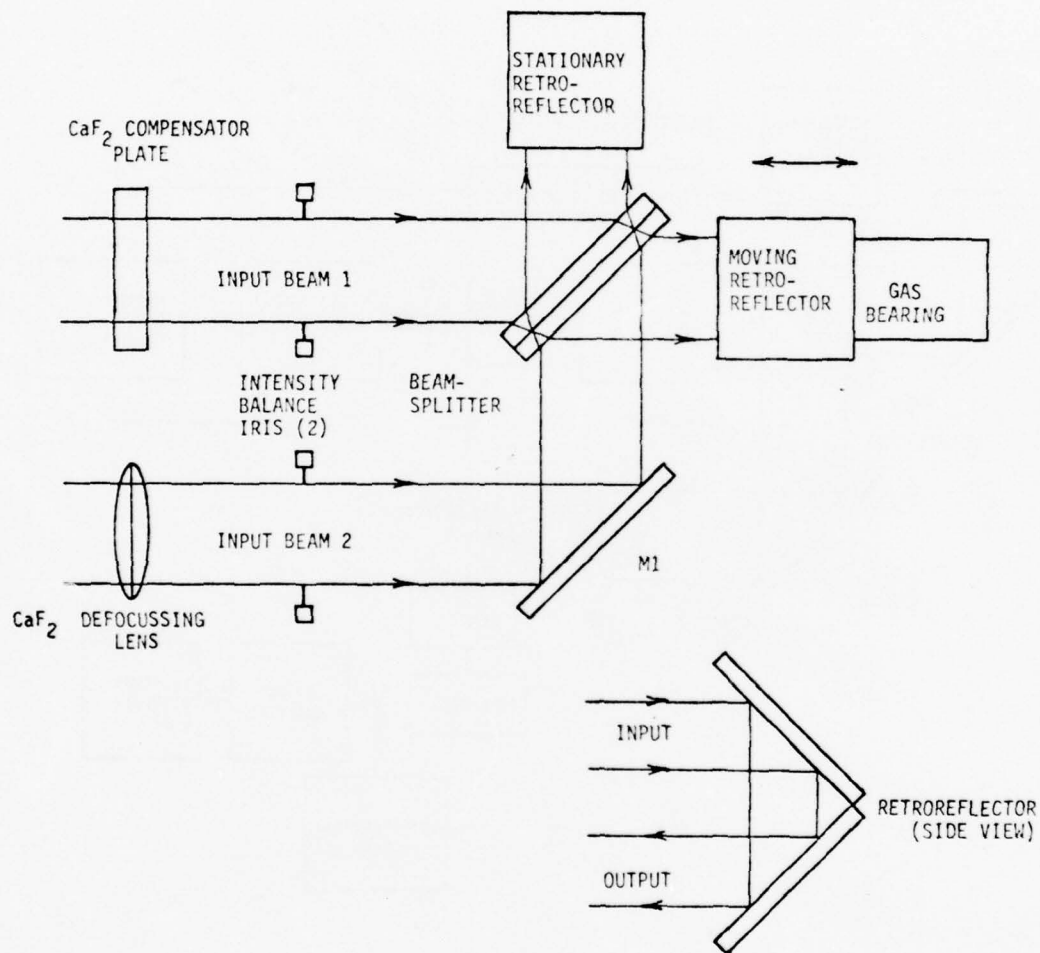


FIGURE 9a: Schematic of double-beam interferometer-spectrometer (upper level).

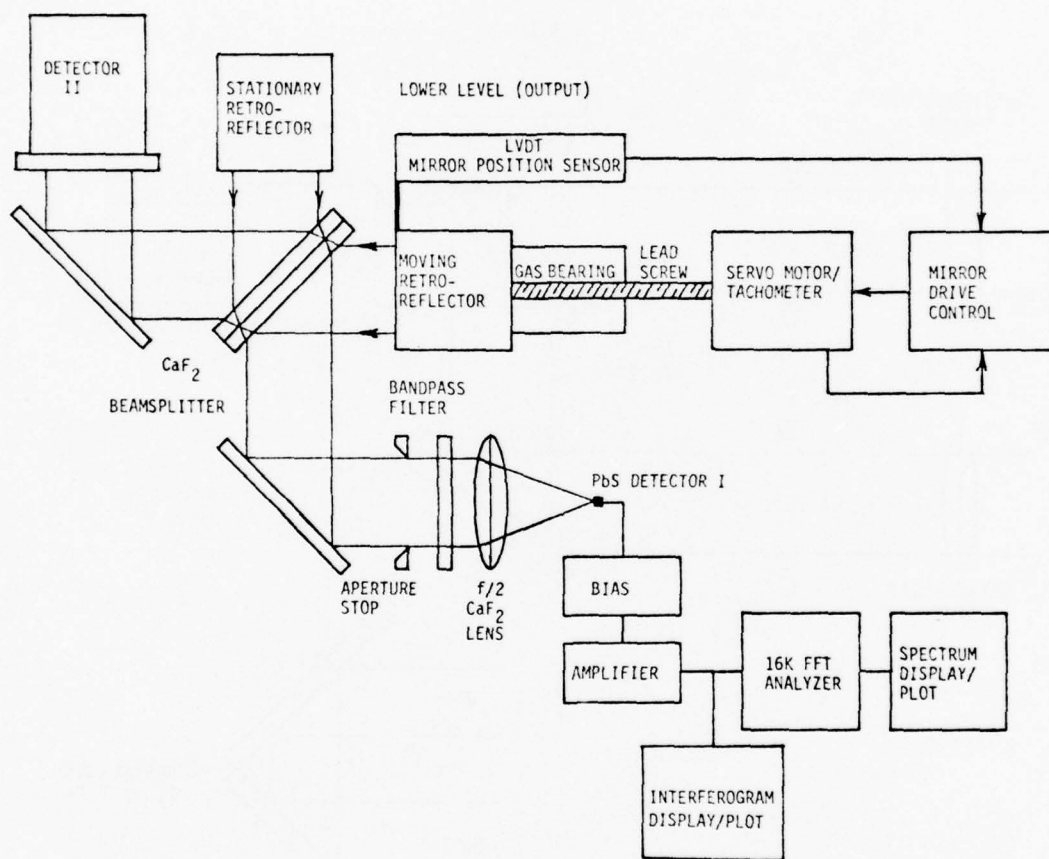


FIGURE 9b: Schematic of double-beam interferometer-spectrometer (lower level).

adjustable iris aperture stops. Each beam is then incident, from opposing directions, on a 7.5 cm diameter beamsplitter-compensator consisting of two parallel plates of CaF_2 between which is sandwiched a thin film of Si. The transmission of the beamsplitter as a function of wavelength, for 0° incidence angle, is shown in Figure 10. The transmitted and reflected beams are both directed to roof-type retroreflecting mirrors. One of the two retroreflectors is movable; both displace the beam down to the lower level of the interferometer.² Roof-type retroreflectors were selected because (1) the beam is reflected by 180° , independent of small tilts of the retroreflectors about two of its three axes of rotation, and (2) the use of roof retroreflectors allows a more compact interferometer than an alternate "cat's eye" design. The mirrors in the retroreflectors, as well as all other reflecting surfaces in the interferometer, were gold coated. The interferometer optics and beamsplitter have been designed for use in the wavelength range 1-10 μm .

In the lower level of the interferometer, the beams are again partially reflected and partially transmitted by the beamsplitter, and a portion of the radiation that enters beam 1 arrives at detector I. The complementary fraction of the radiation is directed to detector II. The detector consists of a PbS cell onto which the beam is focused by a 2.5 cm diameter, f/2 CaF_2 lens. The sensitive area of the detector is 0.25 mm x 0.25 mm. Ambient temperature PbS detectors were used for these measurements because of the ease with which detector size, a BOSS measurement parameter, could be varied. Each detector assembly also contains a spectral filter which limits the overall bandpass of the system. The spatial background suppression data were obtained with a 2.1 μm to 2.5 μm interference filter. This bandwidth was selected so as to minimize atmospheric absorption effects on the

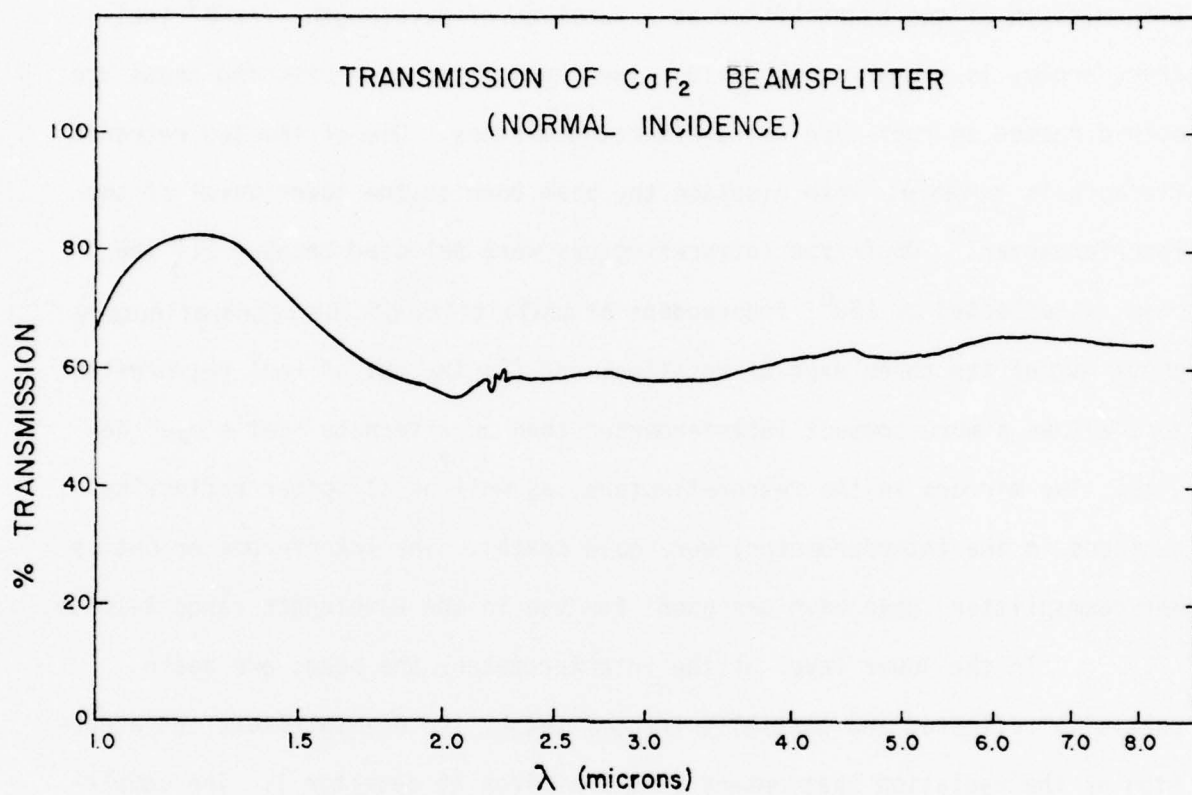


FIGURE 10: Transmission of CaF_2 beamsplitter as a function of wavelength at normal incidence angle.

measurements. Spectral measurements were made with either a silicon or germanium window in place of the filter.

There are numerous degrees of freedom for adjusting and aligning the optical components. The moving retroreflector is mounted on a micrometer adjustable X-Y-Z translation stage. The two mirrors in each retroreflector can be separately aligned. The orientations of each of the other mirrors in the interferometer as well as the positions of the beamsplitter, the fixed retroreflector and the detectors are also adjustable.

As the retroreflecting mirror is moved, monochromatic radiation that enters beam 1 and arrives at detector I will be modulated sinusoidally (see § 2). The modulation rate is proportional to the frequency of the incident radiation and to the speed of the mirror. For a range of wavelengths entering the interferometer in beam 1, a maximum in intensity will be recorded in detector I when the path length to the moving retroreflector equals the path length to the fixed mirror (zero path difference). (See § 2 for a detailed discussion of the optical paths through the interferometer.) Radiation which enters beam 2 and arrives at detector I is also modulated as the retroreflector moves. If the two beams 1 and 2 are equal (i.e., optical axes viewing the same direction, balanced intensities, etc.) the modulations will be 180° out of phase and will yield a DC signal. An imbalance in the two beams, as viewed by detector I, will result in a modulation amplitude proportional to the imbalance.

3.1.2 Mechanical Design

All of the optical components of the interferometer are mounted to an aluminum tooling plate of dimensions 20" x 36" x 1" (Figure 8). The tooling plate is supported above a granite optical bench by extruded aluminum

beams. Vibration damping of the table is provided by Firestone air mounts between the table legs and the laboratory floor.

The retroreflector drive which is mounted below the interferometer base plate is shown schematically in Figure 11. The drive, based on a design that utilizes a precision air-bearing (Dover Instruments, Inc.), a precision lead screw (Precision Thread Grinding), and servocontrolled motor (Torque Systems), has proved very successful. The system has been tested for a mirror travel distance of 1 cm (see § 4), and will be used in the future with a 10 cm travel. To incorporate the 10 cm mirror travel requires only translation of the retroreflectors to other mounting holes that are already provided on the mounting plate.

The speed of the motor is controlled by a servo-system shown schematically in Figure 12. The mirror position is controlled by the ramp output from a waveform generator. The errors in the instantaneous position and speed of the mirror are then fed back into the servo-amplifier to maintain constant mirror velocity.

Several of the opto-mechanical components of the system are completely interchangeable for purposes of checking the balance and symmetry of the system. These include the detectors, detector mounts, retroreflecting mirrors, lens mounts, iris diaphragms, and gas cells.

3.1.3 Laser Reference

A He-Ne laser ($\lambda 6328 \text{ \AA}$) is mounted to the interferometer to provide an absolute retardation reference (Figure 8). The laser beam traverses basically the same optical path as that for beam 2 with the exception of bypassing the first mirror (M1, Figure 9a), and returns to its own silicon

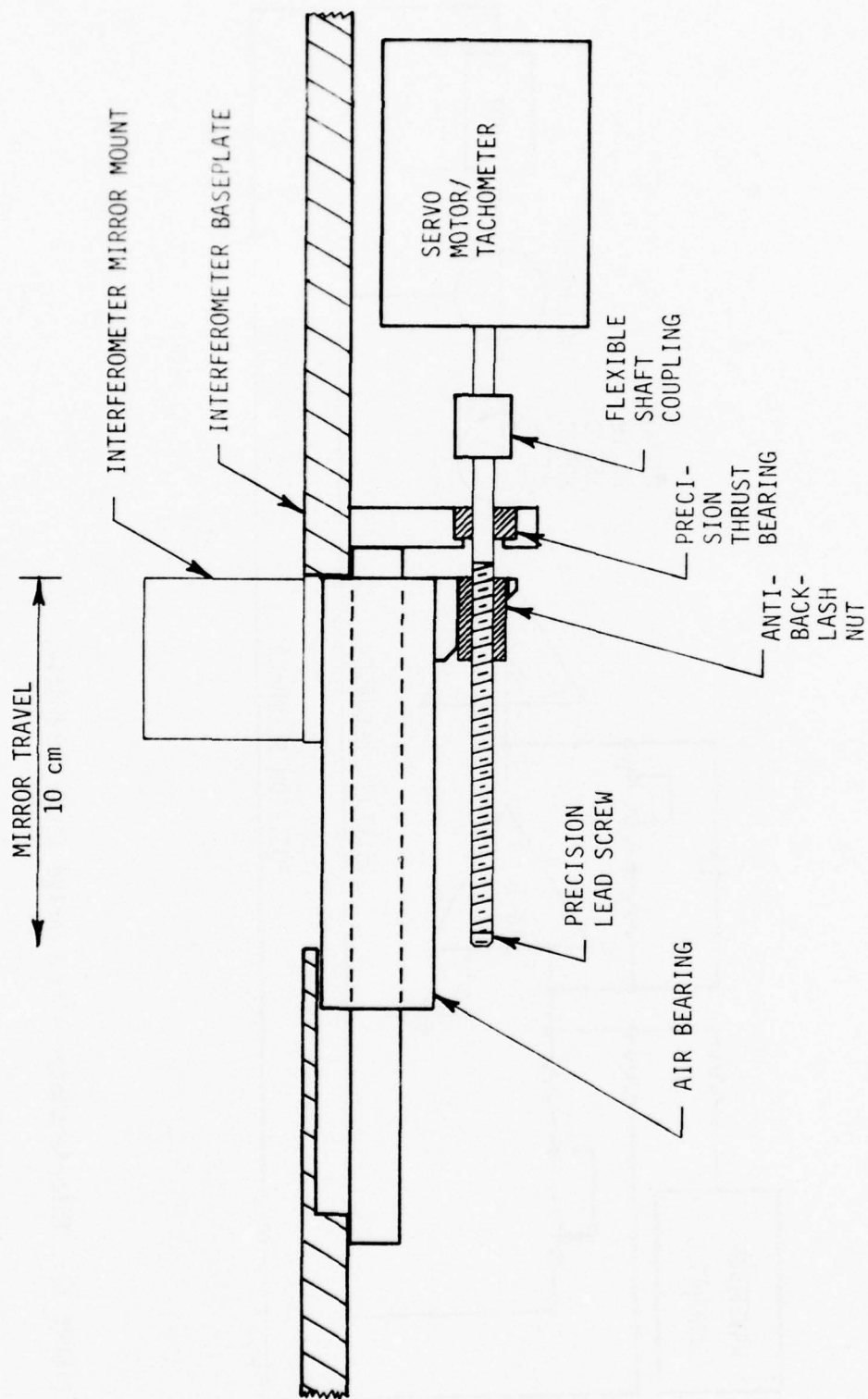


FIGURE 11: Interferometer mirror-drive mechanical diagram.

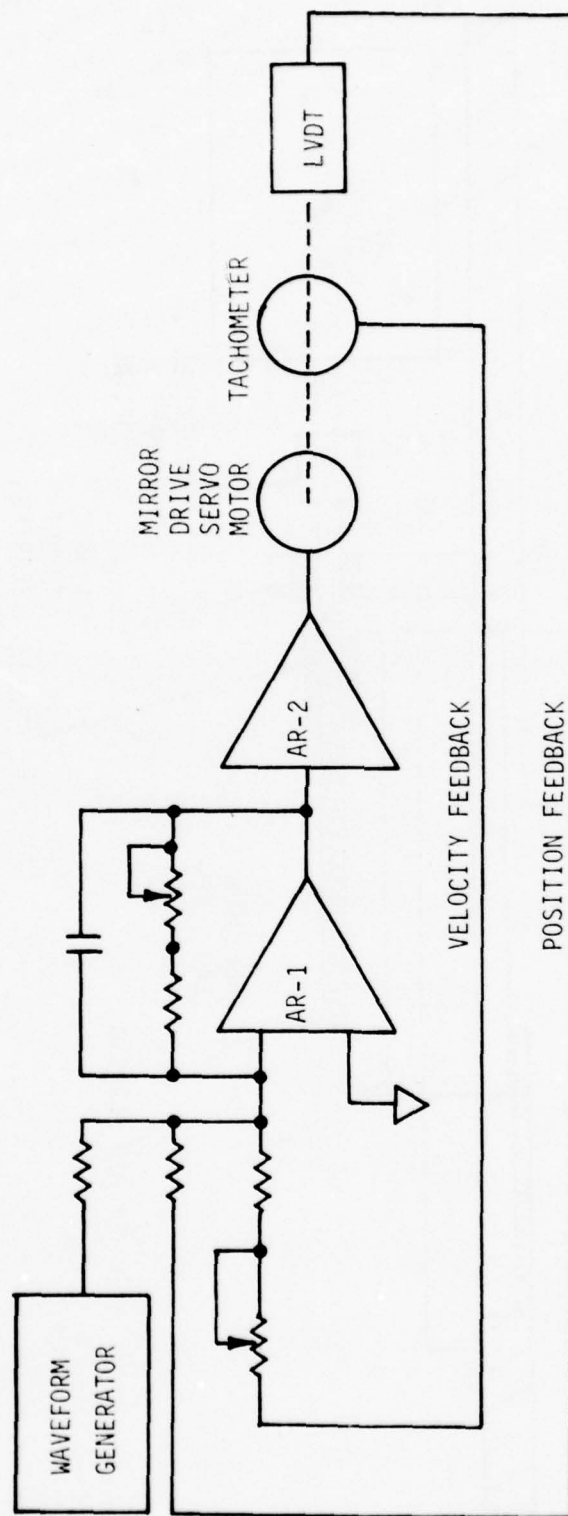


FIGURE 12: Interferometer mirror-drive servo schematic.

detector-amplifier. The laser beam utilizes one corner of the retroreflecting mirrors and thus avoids mixing the laser light with the signal entering the principal detectors of the interferometer. Provisions have also been made to monitor the position of the opposite corner of the retroreflectors, during a scan, to ensure that there are no spurious angular motions of the mirror during scans.

3.1.4 Alignment Procedure

Initially, the beam splitter and the two retroreflectors are aligned with an autocollimator. The system is next brought into finer alignment visually using both monochromatic and white light sources and observing the fringe patterns. Adjustments are made until the fringe patterns of concentric rings are centered on the optical axis of the interferometer.

The two input beams are then co-aligned by adjusting M_1 . Fine alignment adjustments are made with the detector in place and both beams of the interferometer viewing a diffuse light source. When the ratio of single-beam to double-beam interferogram amplitudes at zero path difference is maximized, the interferometer is aligned. In practice the maximum value of this ratio was approximately 100.

3.1.5 Interferometer Configurations

The interferometer can be used in three different modes. (i) The single-beam mode (with one of the two beams blocked) is used to obtain spectra of remote sources. (ii) The double-beam mode with a tailored modulation transfer function is used to obtain spectra of remote localized sources in the presence of a spatially structured background. (iii) The double-beam and single beam modes can be used to measure the absorption (and transmission) spectra of laboratory gas samples. In this configuration, the sample is

placed directly in one of the beams and light from an external source is viewed through the sample. The gas cells shown in Figure 8 are used for this mode.

3.2 The Data System

The data system for the interferometer-spectrometer is shown schematically in Figure 13; some of the key elements are pictured in Figure 14. As the retroreflecting mirror is driven in linear motion, the signal from the detector is amplified and filtered through a low-pass antialiasing filter having a 120 db/octave roll-off. Simultaneously, the laser reference detector electronics sense positive-going zero-crossings and trigger a CORDIC 16K FFT analyzer (Shumway Bros; design rights acquired from Computer Information Systems, Inc.). The FFT analyzer then samples the filtered interferometer detector output, A/D converts the signal to a 12 bit word and stores the result as one input point of a 16K point interferogram. The analyzer has the capability of transforming 32K words per second.

While the interferogram is being read into the CORDIC 16K FFT analyzer, the data are transformed and an 8 K-point amplitude spectrum is outputted for display or plotting. Real or imaginary transforms can both be displayed. The analyzer has the capability of performing a running average of output spectra for a range of selectable averaging times. At the present time, a full double-sided interferogram is inputted; in the future, a white light reference source will be incorporated into the interferometer to provide a zero path difference reference that will enable the analyzer to process single-sided interferograms. Because the phases of the various components in the interferogram are a very slowly varying function of

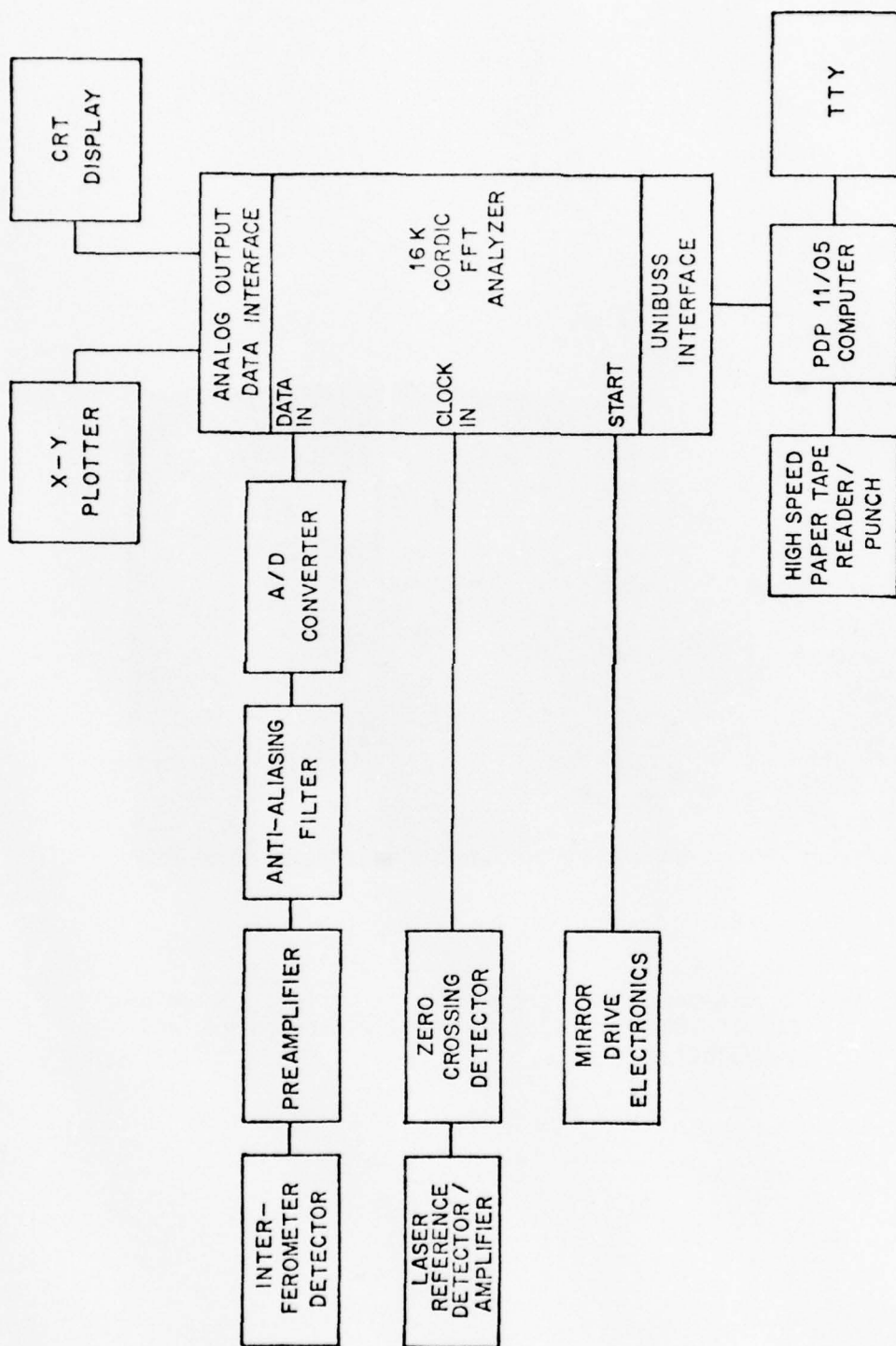


FIGURE 13: Double-beam interferometer laboratory data system.



FIGURE 14: Double-beam interferometer data system, including CORDIC 16K FFT analyzer, PDP 11/05 computer, and x-y plotter.

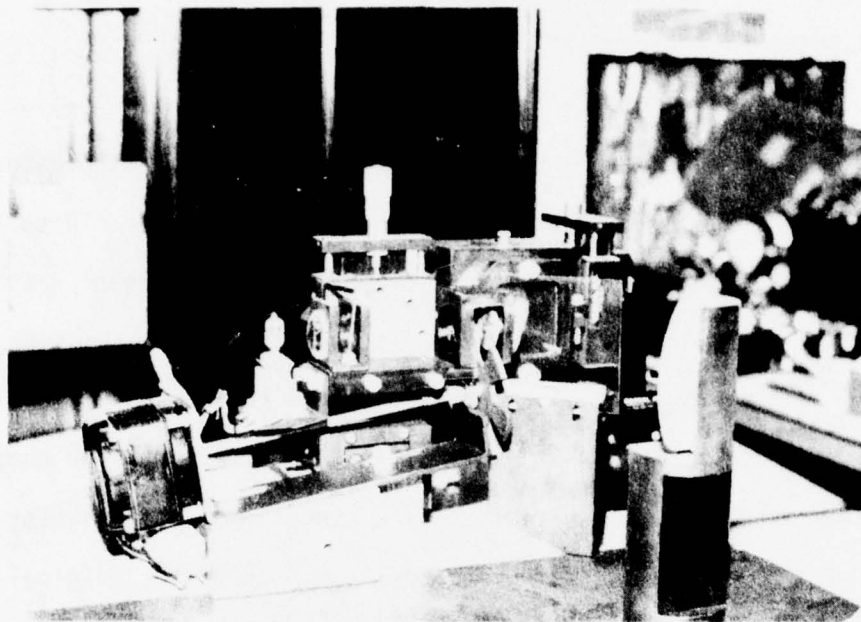
frequency, one can use this information to recover nearly N spectral points from an N -point interferogram¹².

Spectra and interferograms are displayed in several ways. Most of the spectra shown in § 4 were produced directly on the X - Y plotter (Figs. 13 and 14); others were computer-plotted using the analyzer digital data output. Interferograms are usually displayed on a CRT screen (see Fig. 17).

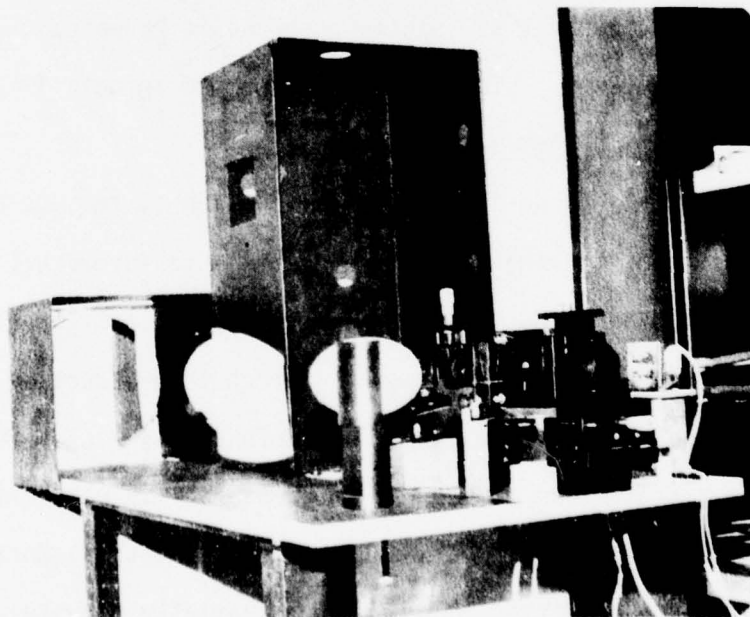
The 16 K CORDIC analyzer can also be used to perform much longer transforms such as would be obtained from data with 0.1 cm^{-1} resolution. A long data train (e.g., 2.6×10^5 points) would be read into the computer and stored. The data train is multiplied by a sinusoid of a particular frequency ν_0 and then summed into coarser bin sizes (e.g., 16 of the original interferogram bins). The compressed data train is then transformed with the CORDIC analyzer in the usual way. The result is a 16K segment of the high resolution spectrum starting at ν_0 . This procedure is repeated until the entire transform is complete. This method is discussed in detail in reference 13.

3.3 The Test System

A special-purpose test and calibration system, to measure the spectral and spatial filtering properties of the interferometer, has been designed and constructed. The system is pictured in Figure 15 and shown schematically in Figure 16. A "point source" is produced by a pinhole, illuminated by a tungsten-halogen lamp, in the focal plane of an 8" diameter f/5 collimating mirror. The mirror views the pinhole by reflection from an elliptical flat (to remove the light sources from the optical path to the interferometer), and a beamsplitter that allows a spatially structured source to be



Side view showing beamsplitter, chopper wheel assembly and focal plane light sources.



Front view showing f/5 primary mirror, elliptical flat and focal plane light sources.

FIGURE 15: Laboratory test system.

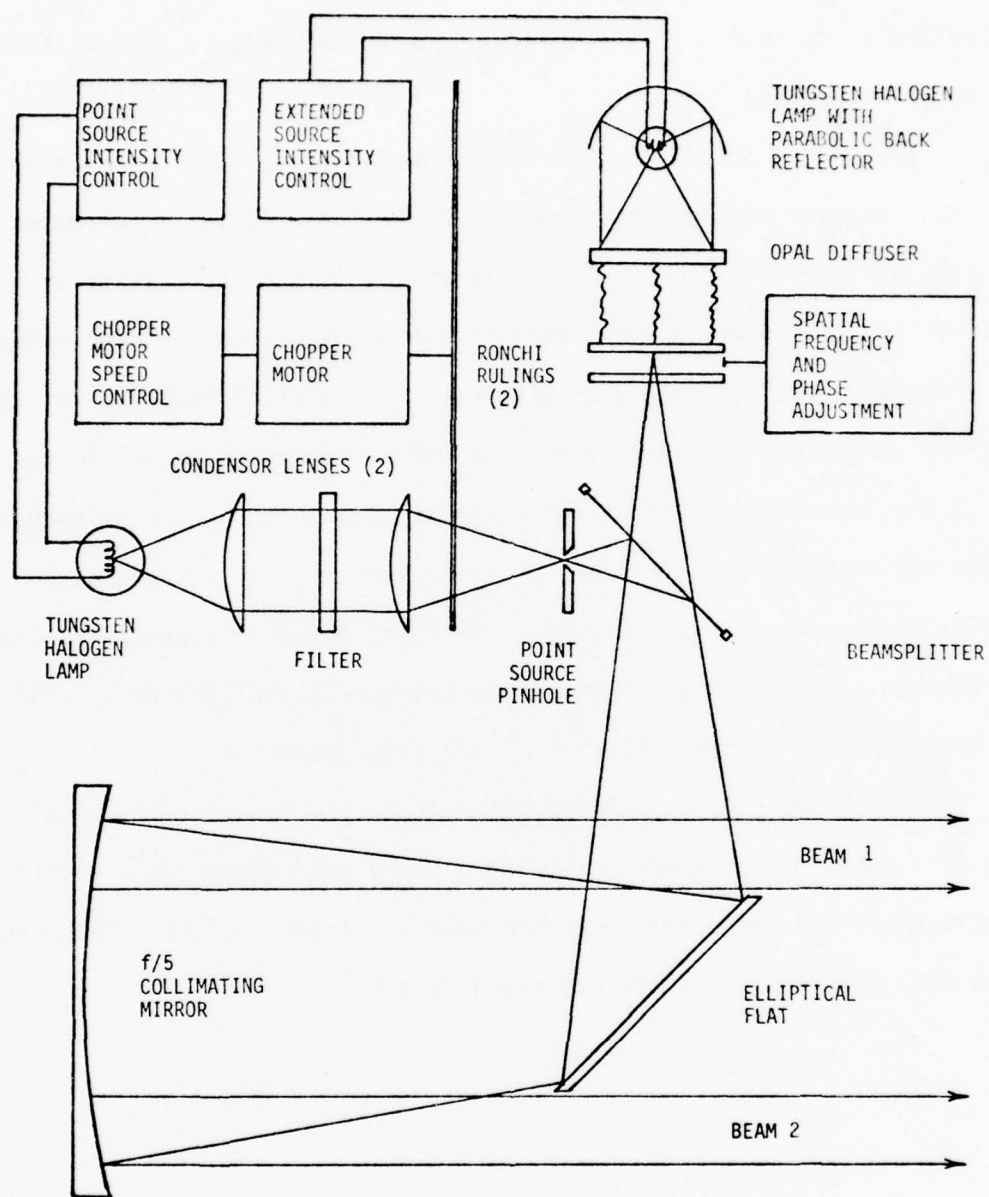


FIGURE 16: Schematic of laboratory test system.

superimposed in the focal plane (Figure 16). Spectral structure can be added to either the point source or the spatially structured source with filters of a variety of materials.

The second source in the focal plane of the mirror is designed to measure the response of the interferometer to various spatial frequencies in a spatially structured background. At present, this source consists of a pair of Ronchi rulings whose Moiré pattern can be described as a two dimensional plane wave with a triangular waveform. The spatial frequency of the wave can be varied continuously from DC to high frequencies above the response of the instrument. The phase of the wave can also be varied either by adjusting the relative positions of the two rulings, or by a translation stage that shifts the pair of rulings. The Moiré pattern is partially transmitted through a beamsplitter where it is subsequently collimated by the $f/5$ mirror and projected in the direction of the interferometer.

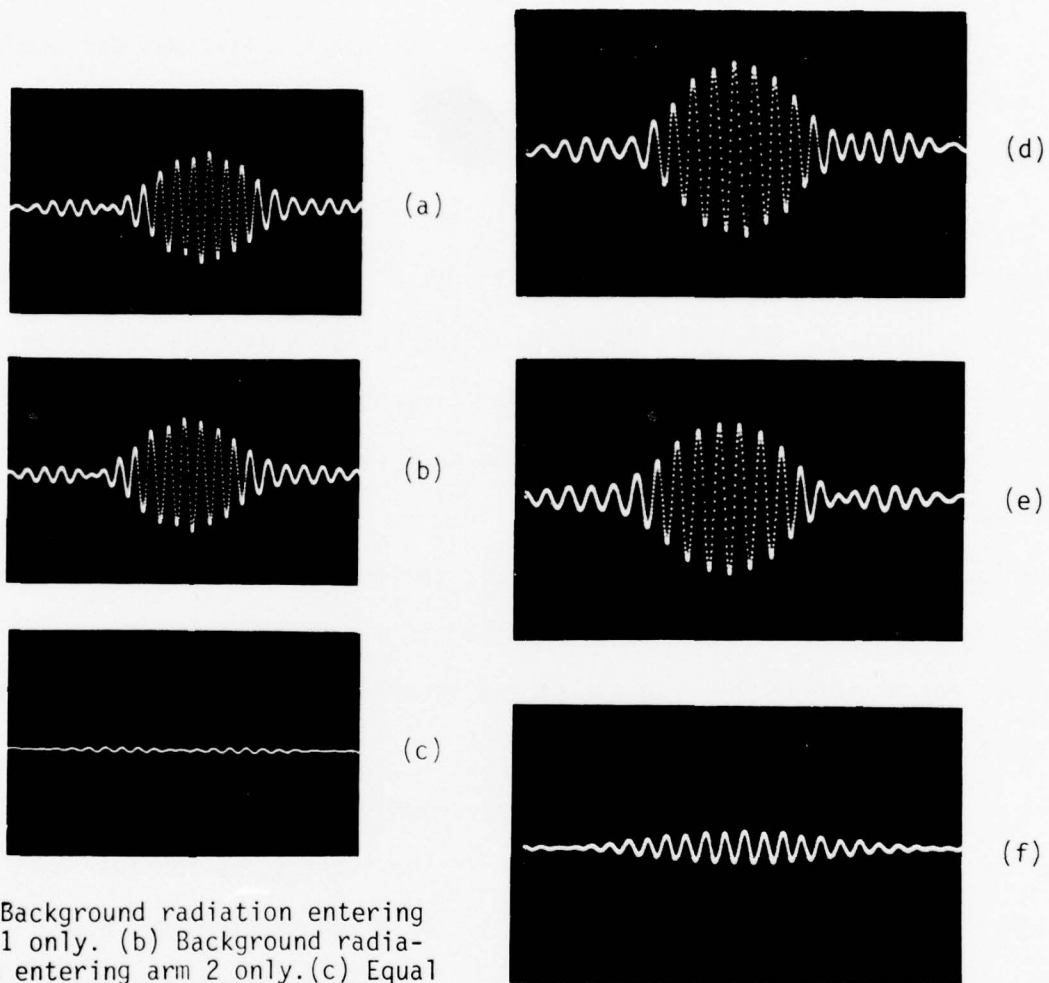
Both beams of the interferometer thus view identical "scenes" consisting of a point source superimposed on a plane wave of variable spatial frequency; these two components may each have different spectra. The results of tests with this apparatus are presented in § 4.

4. LABORATORY TESTS AND DEMONSTRATIONS

The Visidyne double-beam interferometer-spectrometer was designed especially to enhance the detectability of small localized sources viewed against a spatially structured background in the infrared region of the spectrum. The spectral information inherent in the interferometer also allows for additional enhancement of the signal-to-noise if the localized source has a different spectral signature than that of the background. The technique of using a double-beam interferometer, with a tailored modulation transfer function to suppress a spatially extended background, while responding well to localized sources, is discussed in detail in § 2. The design and fabrication of the laboratory double-beam interferometer-spectrometer and all its subcomponents are discussed in § 3. Also described in § 3 is the laboratory test apparatus for measuring the response of the interferometer to various spatial and spectral frequencies.

In this section we describe measurements of the spatial filtering properties of the interferometer (§ 4.1) In these tests, we consider only the total response, i.e., the integral of the observed spectrum or, approximately, the amplitude of the zero path difference fringe in the interferogram. In § 4.2 we examine the background suppression as a function of both spatial and spectral frequency. Finally, in § 4.3 some higher resolution spectra (at 1 cm^{-1} resolution) are presented as a demonstration that an interferometer operating as a spatial filter need not sacrifice frequency resolution. (The drive in our interferometer (see § 3) is, however, capable of yielding 0.1 cm^{-1} resolution, and will be so tested in the near future.)

The principal raw data from a given scan of the interferometer is an interferogram. Sample interferograms are illustrated in Figure 17. The



(a) Background radiation entering arm 1 only. (b) Background radiation entering arm 2 only. (c) Equal background fluxes entering both arms.

Point source superposed on a diffuse background. (d) and (e) show the interferograms for the two arms separately, and (f) reveals the point source interferogram after background suppression.

FIGURE 17: Sample interferograms from the double-beam interferometer.

interferogram from beam 1 (focused beam; see Fig. 1) viewing a diffuse background source is shown in Figure 17a, and the corresponding interferogram from beam 2 (defocused beam) is shown in 17b. When both beams are allowed to combine at the detector, the interferogram is as shown in 17c. Because the background is diffuse, both beams have a nearly identical response; however, the interferograms are out of phase with respect to each other by 180° (see § 2, Fig. 2). The signal is thus reduced to nearly a DC level, and the background is thereby suppressed.

When a point source is viewed against a diffuse background, the results are quite different. The interferogram from beam 1 is shown in Figure 17d, and that from beam 2 is shown in Figure 17e. In the double-beam mode (Fig. 17f), the diffuse background is suppressed as discussed above; the interferogram from the relatively weaker point source is quite discernible (note the differently shaped envelope). This is a result of the fact that beam 1 and beam 2 respond very differently to a point source, and the interferogram is therefore not suppressed (i.e., not reduced to a DC level).

In the remainder of this section, we show only the spectra, which are computed as Fourier transforms of the interferograms. The raw data, however, in each case are interferograms of the kind shown in Figure 17.

4.1 Spatial Filtering Properties

The point spread function of beam 1 (focused beam) and the point spread function of beam 2 (defocused beam) were measured separately. The point light source in the laboratory test apparatus (Fig. 16) was used with a chopper wheel to modulate the signal. (The retroreflectors were at rest during the test, and hence there was no modulation of the signal due to varying path differences.) The measured point spread functions for the two beams

are shown in Figure 18; these include the effects of the CaF_2 defocusing lens, the detector lens and its aberrations, and the finite size of the detector. The ratio of peak responses for the focused to defocused beams is ~ 3.3 . We emphasize, however, that the "areas" under both curves [i.e., $\int I(\theta) 2\pi\theta d\theta$ where $I(\theta)$ is the appropriate point spread function] are equal.

The modulation transfer function (MTF) for each of the two beams (1 and 2) as well as the effective MTF for the system (1 minus 2) were computed by taking a Bessel transform of the point spread functions shown in Figure 18. Specifically, we carried out the following integral:

$$\text{MTF}(K) \propto \int I(\theta) J(2\pi K\theta) 2\pi\theta d\theta \quad (8)$$

where J is a zero order Bessel function and K is the spatial frequency. The results are shown in Figure 19. Note that, as expected, the MTF for the defocused beam falls off at the higher spatial frequencies considerably faster than the MTF for the focused beam. The system MTF, (applicable when the interferometer is used in the double-beam mode) has a value of 0 at $K=0$, exhibits a nearly linear rise for $K \lesssim 0.5$ cyc/deg, peaks at ~ 0.7 cyc/deg, and is followed by a decay to zero at $K \sim 2.5$ cyc/deg. Thus, the present optics yield the greatest sensitivity for sources with an angular extent of $\sim 0.4^\circ$ - 1.2° .

The sensitivity of the double-beam interferometer to various spatial frequencies was directly measured with the laboratory test source discussed in § 3 (Fig. 16). The pair of Ronchi rulings in this source was adjusted to yield a Moiré pattern with a specific spatial frequency (as well as the higher harmonics associated with the triangular wave form). The phase of the Moiré pattern was adjusted relative to the optical axis of the interferometer until a maximum in intensity in the central fringe of the

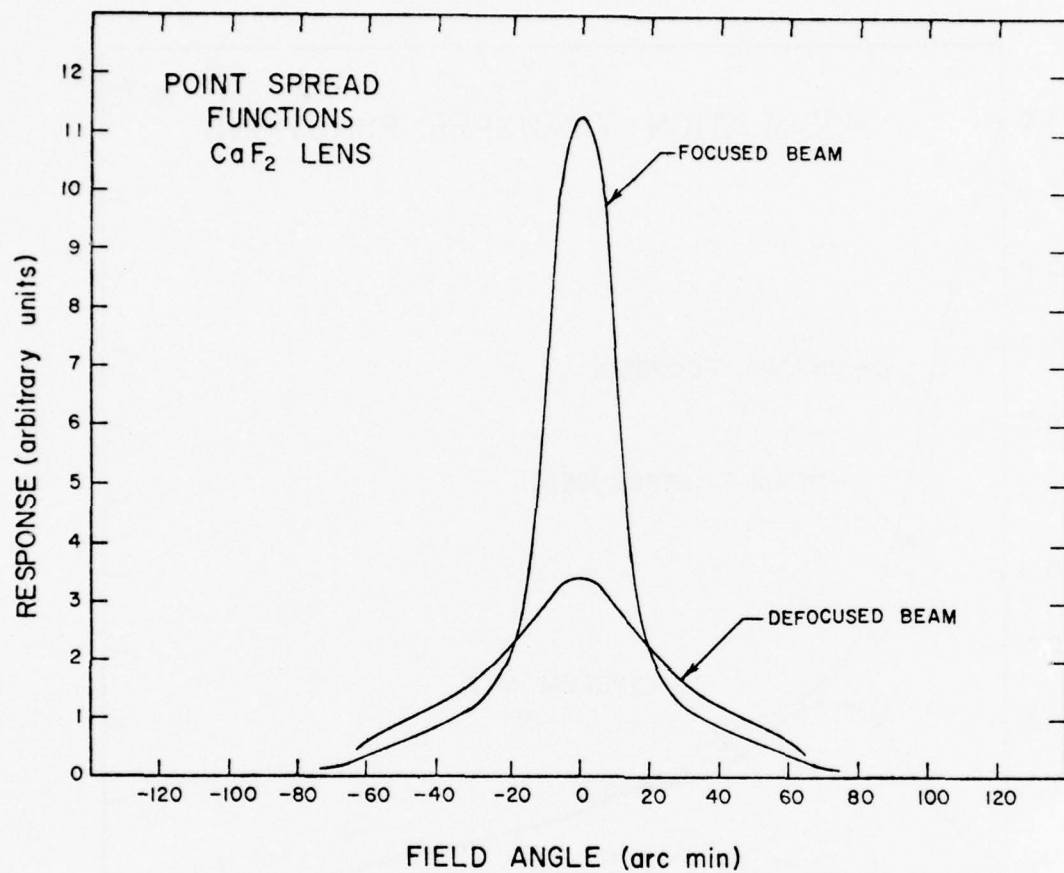


FIGURE 18: Point spread functions for the beams with the CaF₂ defocusing lens and the CaF₂ compensator plate. In each case, the spatial resolution of the detector is included.

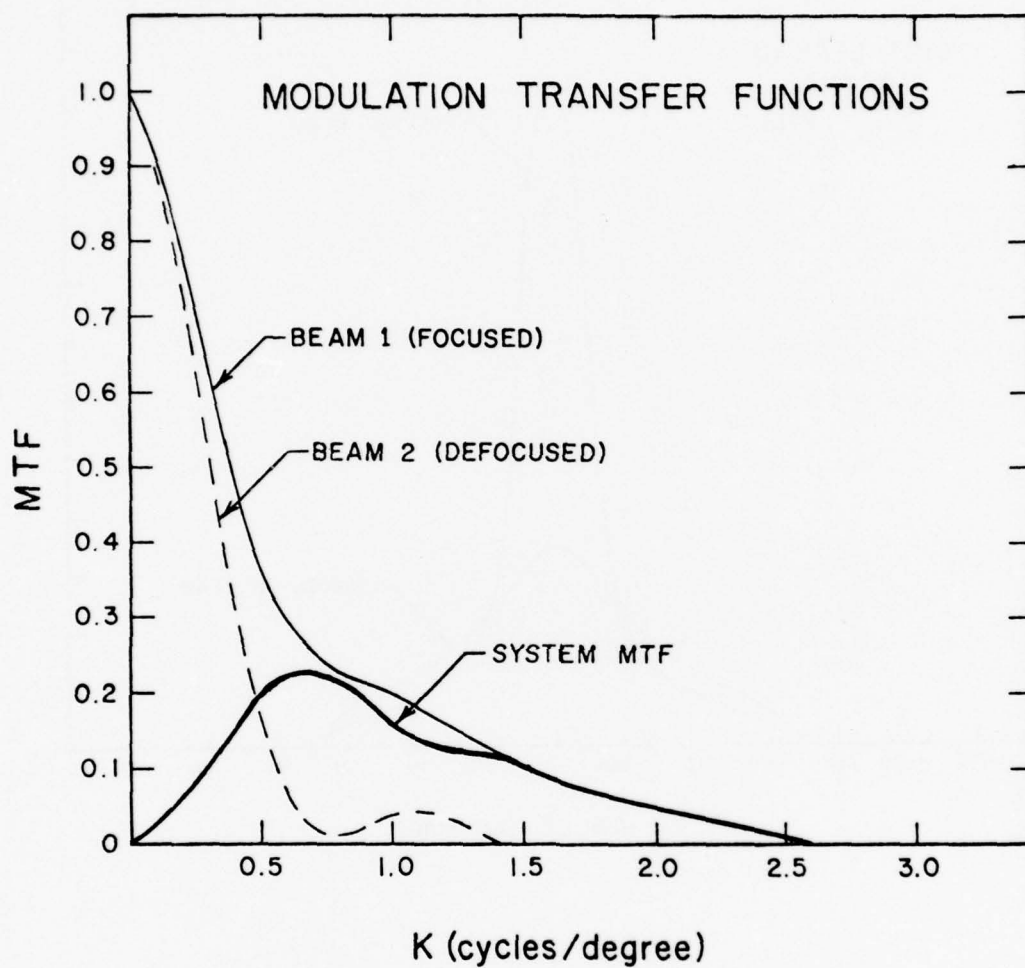


FIGURE 19: Modulation transfer functions for the beams with the CaF_2 defocusing lens and the CaF_2 compensator plate. In each case, the spatial resolution of the detector is included.

interferogram was recorded. At this setting, the interferogram and the transformed spectrum were recorded for both the single-beam and double-beam modes. The phase of the wave was then shifted until a minimum in intensity was obtained, and data were similarly recorded. This procedure was repeated for a number of different values of the spatial frequency K . The response of the interferometer (defined as the spectrum integrated over all frequencies) in the double-beam mode was then normalized to the response of the focused beam alone. The results as a function of K are plotted in Figure 20; the data points rise to a pronounced maximum at $K \approx 0.9$ cyc/deg.

In the above test, the measured response of the interferometer to different spatial frequencies is closely related to the MTF of the system. To see this, we note that the theoretical response of the interferometer to a two-dimensional source with spatial distribution $S(x,y)$ and transform $\tilde{S}(k_x, k_y)$ is (ref. 10):

$$D(x,y) \propto \frac{1}{2\pi} \sum_{\text{odd}} S(k_x, k_y) \text{MTF}(k_x, k_y) e^{ik_x x + ik_y y} dk_x dk_y, \quad (9)$$

(cf. equation 6, § 2). For the triangular waveform produced by the Ronchi rulings,

$$S(x,y) = S_0 [1 + 8/\pi^2 \sum_{\text{odd}} n^{-2} \cos(nk_0 x)]/2 \text{ and} \quad (10)$$

$$\tilde{S}(k_x, k_y) = S_0 \pi [\delta(k_x) + 4/\pi^2 \sum_{\text{odd}} n^{-2} \{\delta(k_x - nk_0) + \delta(k_x + nk_0)\}] \delta(k_y)$$

where k_0 is the fundamental spatial frequency of the Moiré pattern. Therefore $D(x,y)$ can be computed analytically:

$$D(x,y) = S_0 [\text{MTF}(0) + 8/\pi^2 \sum_{\text{odd}} n^{-2} \text{MTF}(nk_0) \cos(nk_0 x)] \quad (11)$$

The ratio of the maximum response in the double beam mode to the single beam mode is then:

$$R(k_0) = \frac{\text{MTF}_{A-B}(0) + 8/\pi^2 \sum_{\text{odd}} n^{-2} \text{MTF}_{A-B}(nk_0)}{\text{MTF}_A(0) + 8/\pi^2 \sum_{\text{odd}} n^{-2} \text{MTF}_A(nk_0)} \quad (12)$$

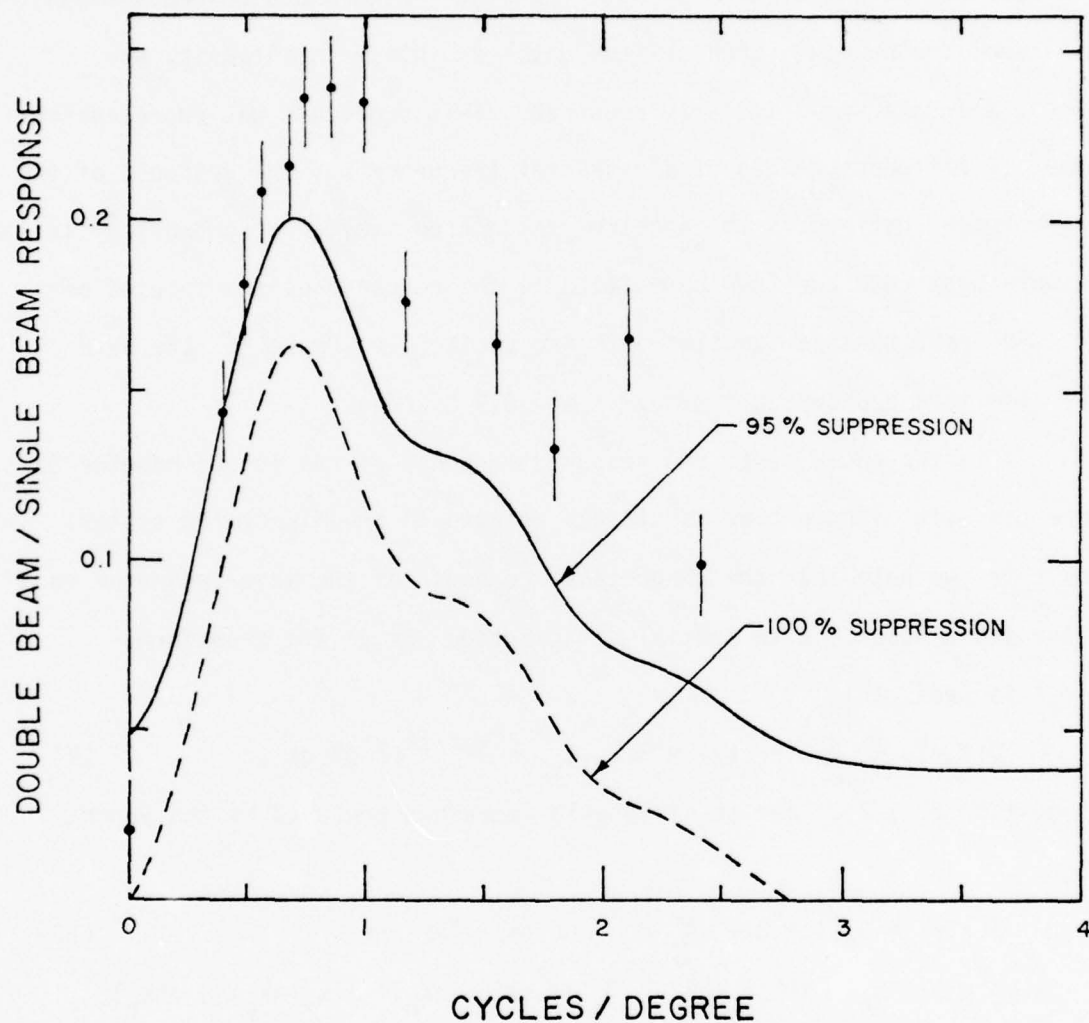


FIGURE 20: Ratio of the double-beam response of the interferometer to the single-beam response, as a function of the spatial frequency of the Moiré pattern. The solid and dashed curves are the expected ratios (eq. 12) for an ideal interferometer with 95% and 100% suppression of the DC background, respectively.

where MTF_A and MTF_{A-B} are the MTFs for beam 1 and beams 1 minus 2, respectively. For the case where $MTF_{A-B}(0)=0$ (perfectly balanced beams), and for those values of nk_0 where $MTF_A(nk_0) \ll MTF_A(0)$:

$$R(k_0) \approx \frac{8}{\pi^2} \sum_{\text{odd}} n^{-2} MTF_{A-B}(nk_0) \approx \frac{8}{\pi^2} MTF_{A-B}(k_0) \quad . \quad (13)$$

Thus, by means of the above computations, the measured ratio, R , of double-beam to single-beam response as a function of spatial frequency can be directly interpreted in terms of the MTF of the interferometer. The dashed curve in Figure 20 shows the expected ratio $R(k)$ computed from equation (12) for the case where the DC component in the spatially structured background is perfectly suppressed (i.e., perfectly balanced beams with $MTF(0)=0$). The solid curve is computed from equation (12) for an imbalance of 5% between the two beams. Note that the data points qualitatively follow the latter curve. The qualitative differences could be due to a combination of the following causes: (i) imperfect alignment between the two beams, (ii) non-uniform illumination of the Ronchi rulings, and (iii) edge effects due to the finite size of the test pattern.

In the future, we plan to replace the simple fringe-pattern source in the test apparatus by more complicated spatial structures (e.g., aerial photographs) that contain an entire spectrum of spatial frequencies. For diagnostic purposes, however, the present use of Ronchi rulings permits a better understanding of the instrument response to specific frequencies.

4.2 Combined Spatial and Spectral Filtering Properties

In the previous section (§ 4.1) we described the spatial filtering properties of the interferometer, and in particular its capability for suppressing low spatial frequencies. In this section we describe how the back

ground suppression of the interferometer-spectrometer is enhanced by utilizing the spectral information inherent in such a device.

A Moiré pattern of a given spatial frequency was produced with the Ronchi rulings, and a relatively low-intensity point source was superimposed by illuminating the pinhole on the complementary side of the beamsplitter. A spectral filter composed of 1.5 mm thick polycarbonate was placed in front of the point source. Thus, the "background" had both a different spectral as well as spatial composition than the weaker point source which was to be detected.

For each of several different spatial frequencies the interferogram and the transformed spectrum were recorded in both the single-beam and double-beam modes. The spectra obtained for three sample spatial frequencies (0, 1.1, and 7 cyc/deg) are shown in Figures 21, 22, and 23.

The response to a uniform background ($K=0$) with point source superposed is depicted in Figure 21. Spectra for the point source plus background are shown for the double-beam and single beam modes; a double-beam spectrum of the background alone is also shown for comparison. The overall spectral shape ($\sim 4000\text{-}5000\text{ cm}^{-1}$) exhibited in the single-beam mode results from the transmission properties of an interference filter located in front of the detector. In the double-beam mode, nearly all of the background radiation is suppressed, while the spectrum of the polycarbonate filter placed in front of the point source is clearly revealed. By contrast, about 75% of the intensity of the point source is retained in the double-beam mode because the source has contributions from all spatial frequencies. (The baseline of this spectrum has been shifted upward in order to separate the curves.) The double-beam spectrum without the point source shows how completely the background is suppressed. For all but a small range of frequencies ($\sim 4100\text{-}4250$

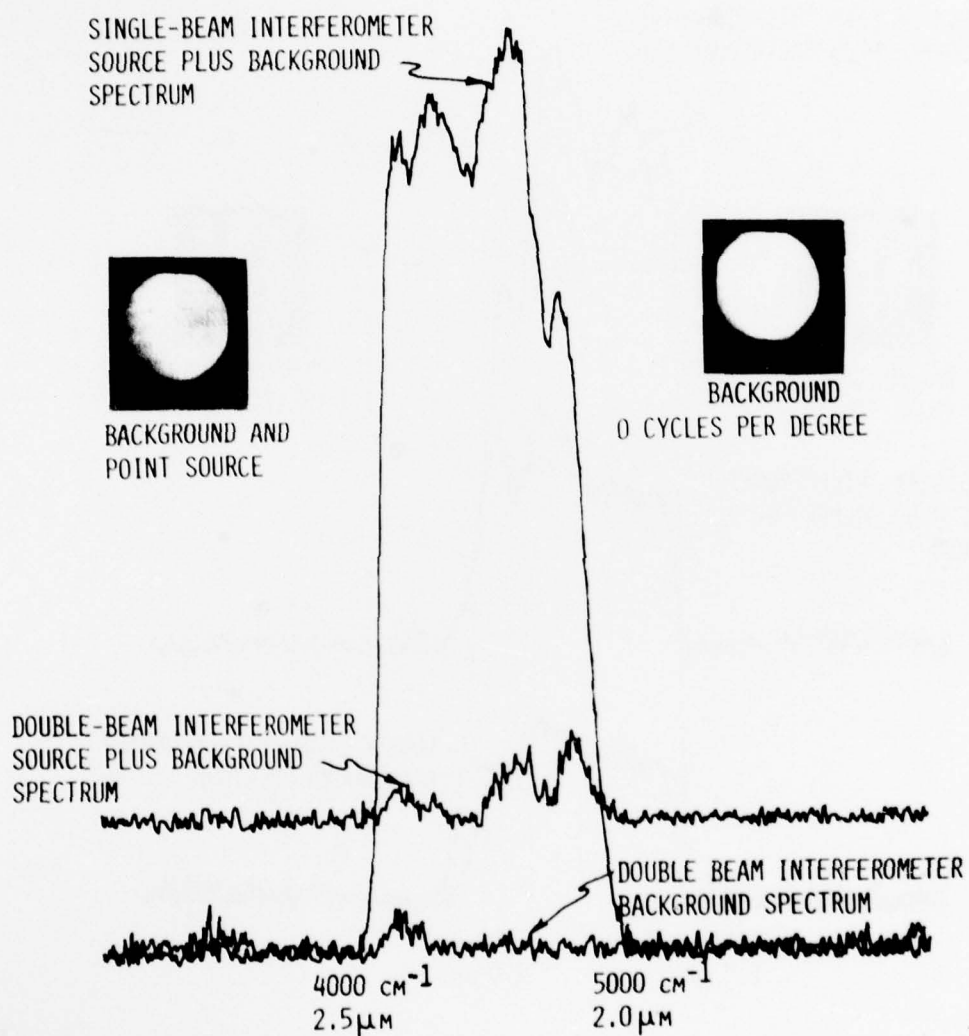


FIGURE 21: Single and double-beam spectra of a point source superposed on a diffuse (DC) background. (The baseline for the double-beam spectrum has been shifted upward in order to separate the curves.) Shown for comparison is a double-beam spectrum of the background alone to demonstrate the high degree of suppression.

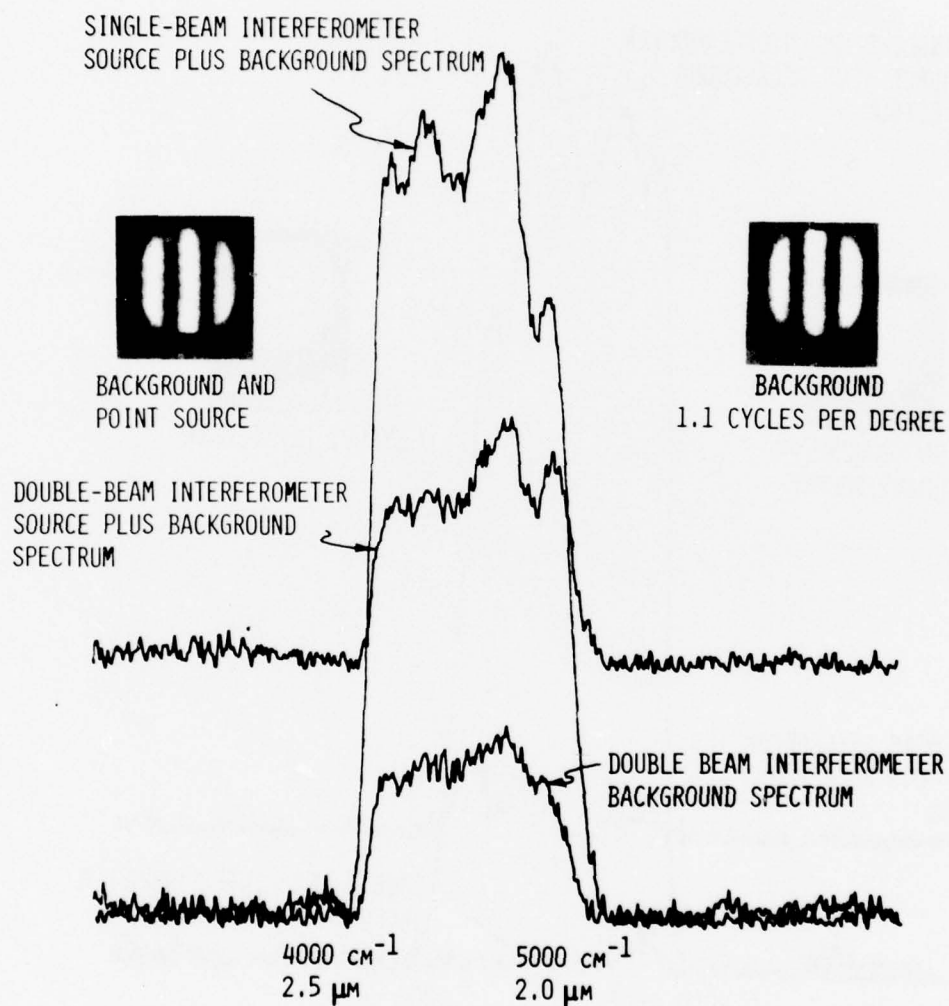


FIGURE 22: Single and double-beam spectra of a point source superposed on a background with spatial frequency 1.1 cycles per degree. Shown for comparison is a double-beam spectrum of the background alone.

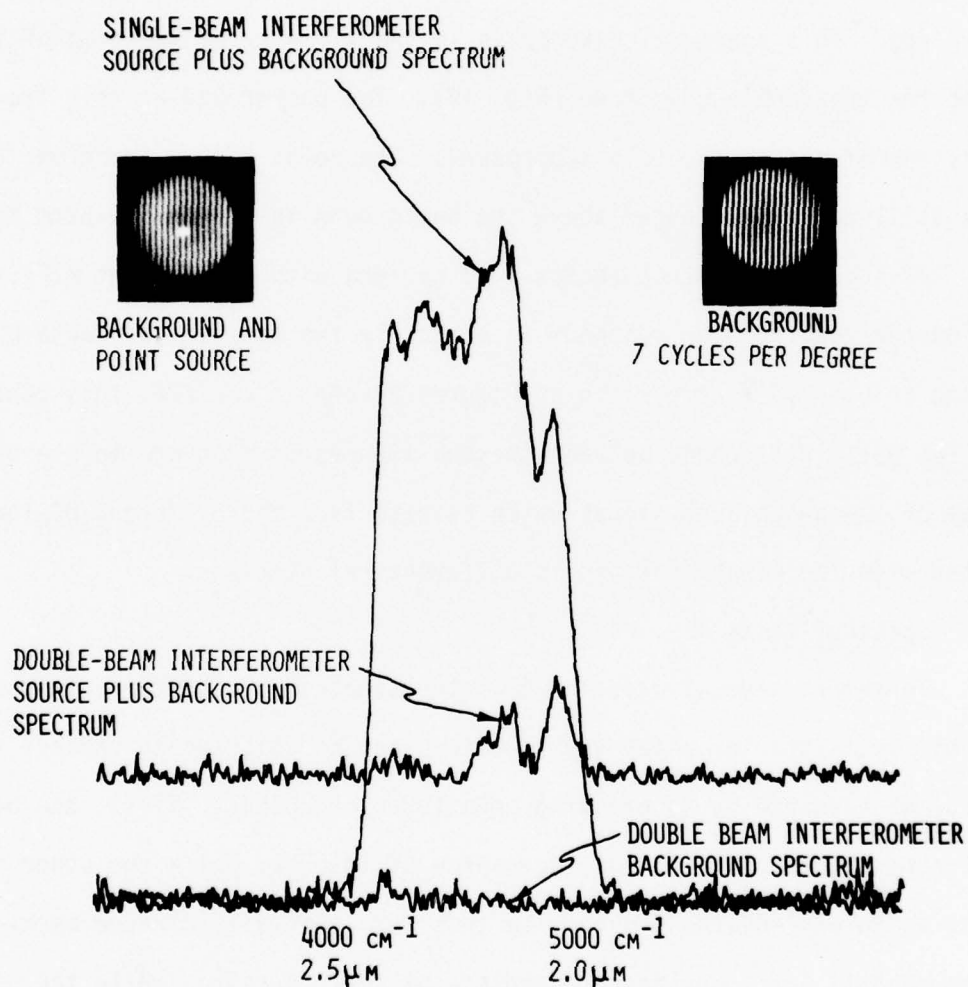


FIGURE 23: Single and double-beam spectra of a point source superposed on a background with a high spatial frequency of 7 cycles per degree. Shown for comparison is a double-beam spectrum of the background alone to demonstrate the high degree of suppression.

cm^{-1}) the suppression ratio is $\approx 100:1$. For a point source whose spectrum is characterized by a narrow line, or a set of narrow lines, the enhancement of signal-to-background over a simple photometer could easily exceed $10^4:1$.

The background was next changed to a fringe pattern of frequency ~ 1.1 cyc/deg. This spatial frequency is in the vicinity of the peak of the MTF curve for the double-beam mode (Fig. 19). The background at this frequency is therefore incompletely suppressed. The point source spectrum, however, is still quite pronounced above the background in the double-beam mode.

At high spatial frequencies ($\gtrsim 3$ cyc/deg with the present MTF), the interferometer-spectrometer responds in virtually the same way as for a DC background (Fig. 19). A comparison of Figures 23 and 21 verifies this conclusion. The basic difference between the two figures is a change in overall intensity of the background signal which results from the different DC levels associated with the Ronchi rulings in different orientations.

4.3 Spectral Tests

There are several ways in which the spectral information, inherent to a double-beam interferometer-spectrometer, can be utilized to enhance the visibility of a source by suppressing unwanted backgrounds. First, one beam of the interferometer is aimed at the source of interest while the other is offset so as to exclude the source. In this way, spatially diffuse background components are suppressed regardless of their spectra, while the higher spatial frequency components in the background can be distinguished by their spectra. Second, different spatial frequency responses (MTF) can be incorporated into the two beams, both of which have the same view direction. Again, spatially diffuse background components are suppressed regardless of

their spectra, while the higher spatial frequency components in the background can be distinguished by their spectra. (see § 4.2) Third, the source may be placed directly into one of the two beams of the interferometer. All spectral components common to both beams (i.e., most non-source background) will be suppressed. The latter technique is not directly applicable to remote sensing problems, but is the most convenient laboratory demonstration of the spectral capabilities of the interferometer.

For these tests, we made use of the interferometer configuration shown in Figure 24. A cell, containing a gas whose absorption spectrum is to be measured, is placed directly in the path of one of the beams. An identical cell (not shown in Figure 24) is placed in the other beam to null any effects due to the first cell. The single-beam and double-beam spectra for the case of air in both cells are shown in Figure 25. The overall spectral shape for the single-beam response is due to the silicon filter (in front of the detector) at short wavelengths, and the PbS detector at long wavelengths; some of the absorption features are due to water vapor in the air. Note the excellent cancellation of the signal in the double-beam mode, as expected (see § 2, Figure 2c). The spectral resolution here is 10 cm^{-1} .

Pure NH_3 vapor at 1 atmosphere pressure is now introduced into one of the cells. The spectrum taken in the single-beam mode is shown in Figure 26. This spectrum represents approximately the transmission of NH_3 vapor multiplied by the smoothly varying sensitivity function of the interferometer.

Most effects of the filter, the water vapor in the air, and any effects other than absorption by NH_3 are easily and effectively removed by a

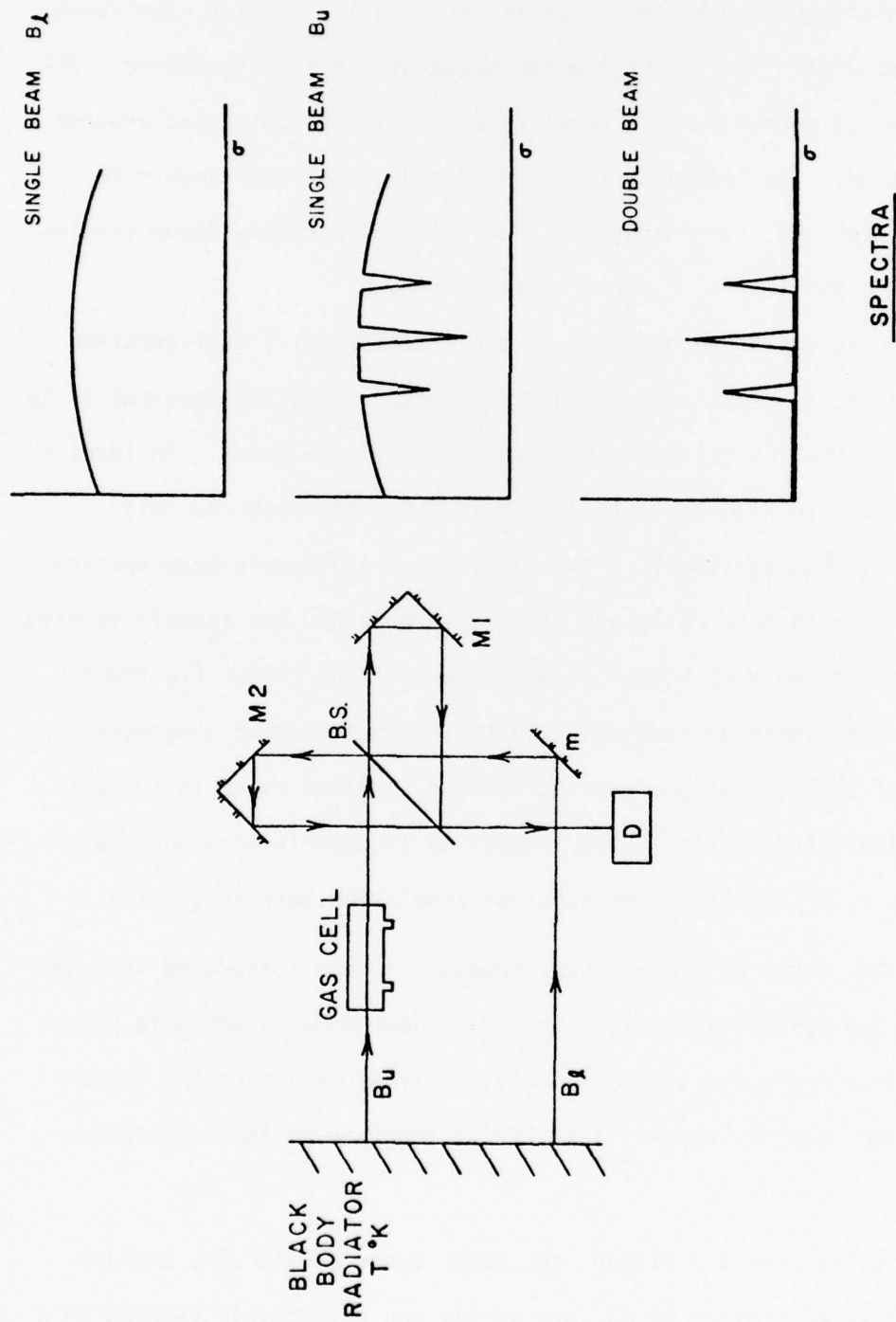


FIGURE 24: Double-beam interferometer configuration for measuring absorption and transmission spectra of laboratory gas samples.

DOUBLE BEAM INTERFEROMETER

RELATIVE SPECTRAL
RESPONSIVITY

$$\delta\sigma - 10 \text{ cm}^{-1}$$

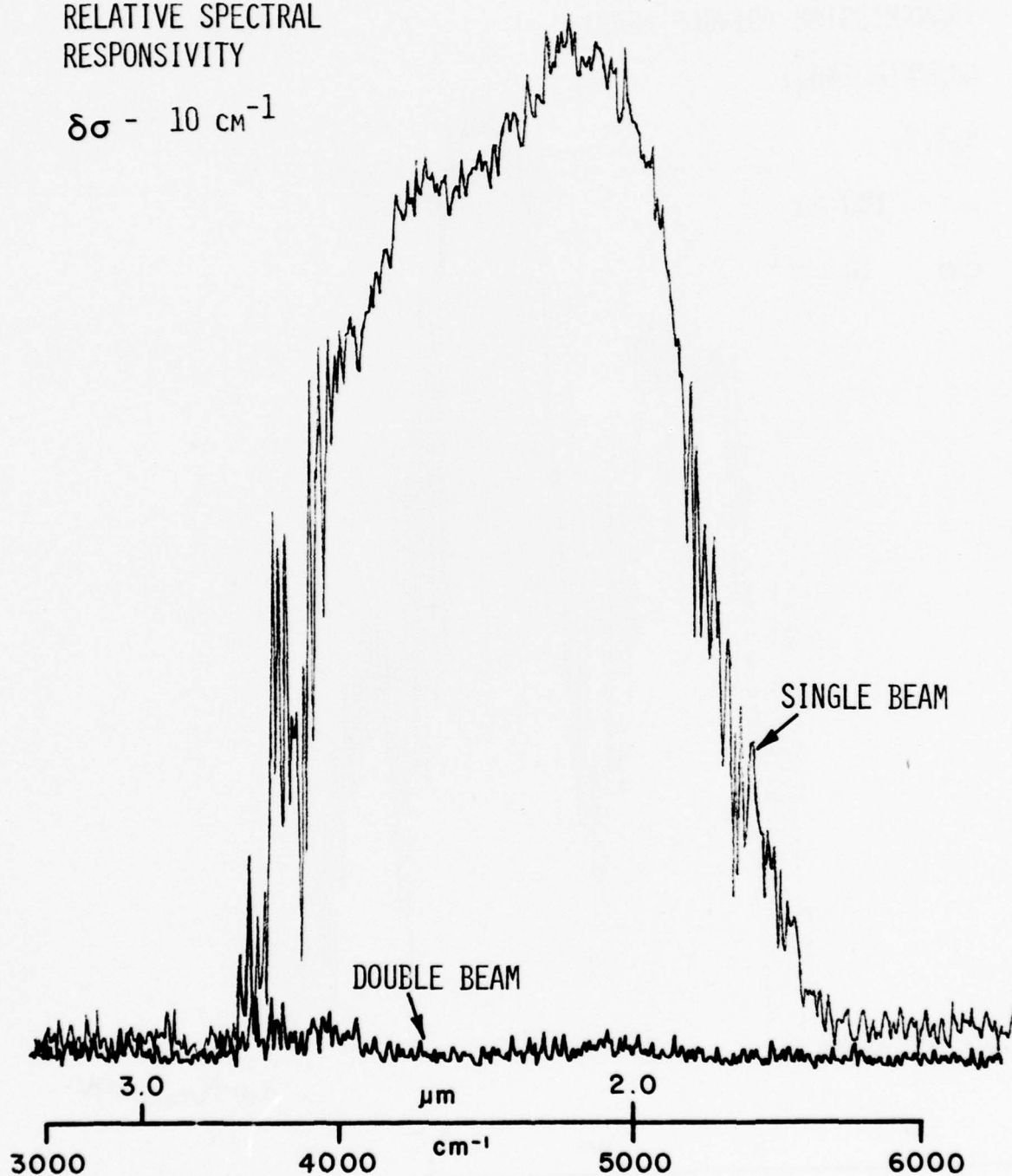


FIGURE 25: Single-beam and double-beam spectra of a broadband light source. The overall response is limited by the Si detector window at short wavelengths, and the PbS detector at long wavelengths. Water vapor absorption features at ~ 3700 and 5300 cm^{-1} are evident.

DOUBLE BEAM INTERFEROMETER
TRANSMISSION (SINGLE BEAM)

AMMONIA (NH_3)

S.T.P.

L - 100 mm

$\delta\sigma$ - 10 cm^{-1}

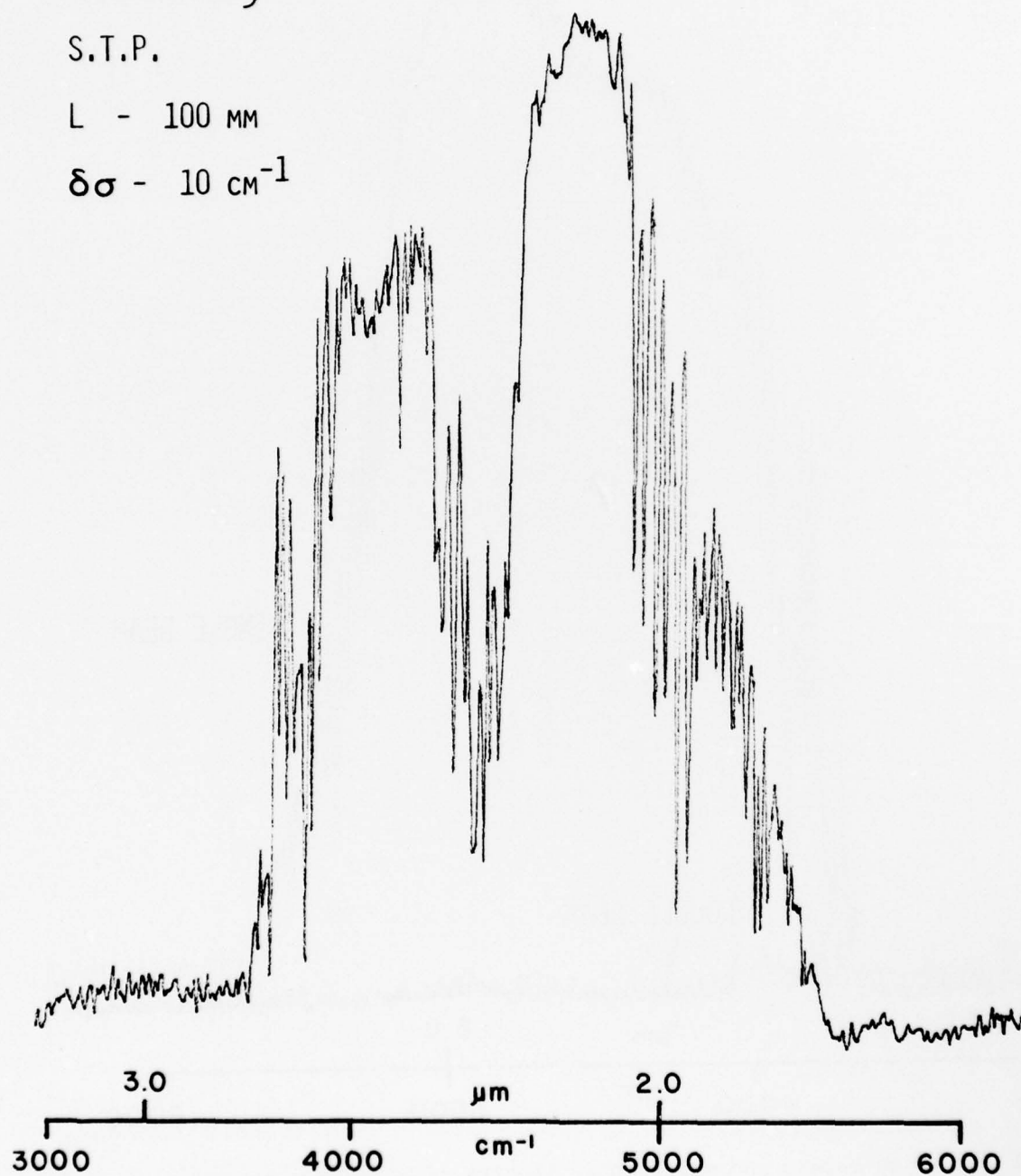


FIGURE 26: Single-beam transmission spectrum of NH_3 vapor.

spectrum produced in the double-beam mode. To see this, let the ideal spectrum recorded in the single-beam mode be $S(\sigma)$ (this includes the source spectrum and the spectral response of the interferometer), and define $T_g(\sigma)$ and $T_c(\sigma)$ as the transmission of the test gas, and the transmission of all other matter (e.g., water vapor, gas cell, etc.) between the light source and the detector, respectively. Then the response in the single-beam mode is:

$$R_{sb}(\sigma) = S(\sigma)T_c(\sigma)T_g(\sigma) \quad (14)$$

while the response in the double-beam mode is:

$$\begin{aligned} R_{db}(\sigma) &= S(\sigma)T_c(\sigma) - S(\sigma)T_c(\sigma)T_g(\sigma) \\ &= S(\sigma)T_c(\sigma)[1 - T_g(\sigma)] \\ &= S(\sigma)T_c(\sigma)A_g(\sigma) \end{aligned} \quad (15)$$

where $A_g(\sigma)$ is the absorption of the test gas. Thus, the double-beam response is the absorption of the gas multiplied by the source spectrum and the absorption spectra of other contaminants. The advantage of this presentation is that all spectral features that are unrelated to the gas, and that are away from regions of significant absorption by the gas, are suppressed.

The results for NH_3 absorption (double-beam mode) are shown in Figure 27. The prominent $(\nu_2 + \nu_3)$ and $(\nu_3 + \nu_4)$ vibration/rotation bands (ref. 14) at $\sim 4450 \text{ cm}^{-1}$ and $\sim 5050 \text{ cm}^{-1}$, respectively, with fine structure down to 10 cm^{-1} are clearly evident. The absorption and transmission spectra are superposed in Figure 28 to emphasize the one-to-one correspondence of the features and to demonstrate their reality.

A similar experiment was performed with a 1.5 mm thick polycarbonate absorber instead of the gas cell. The superposed transmission and absorption spectra are shown in Figure 29. A broad absorption feature for wavelengths greater than $\sim 2.2 \text{ }\mu\text{m}$ ($\sigma \lesssim 4500 \text{ cm}^{-1}$) is clearly evident.

DOUBLE BEAM INTERFEROMETER

ABSORPTION

AMMONIA (NH_3)

S.T.P.

L - 100 mm

$\delta\sigma$ - 10 cm^{-1}

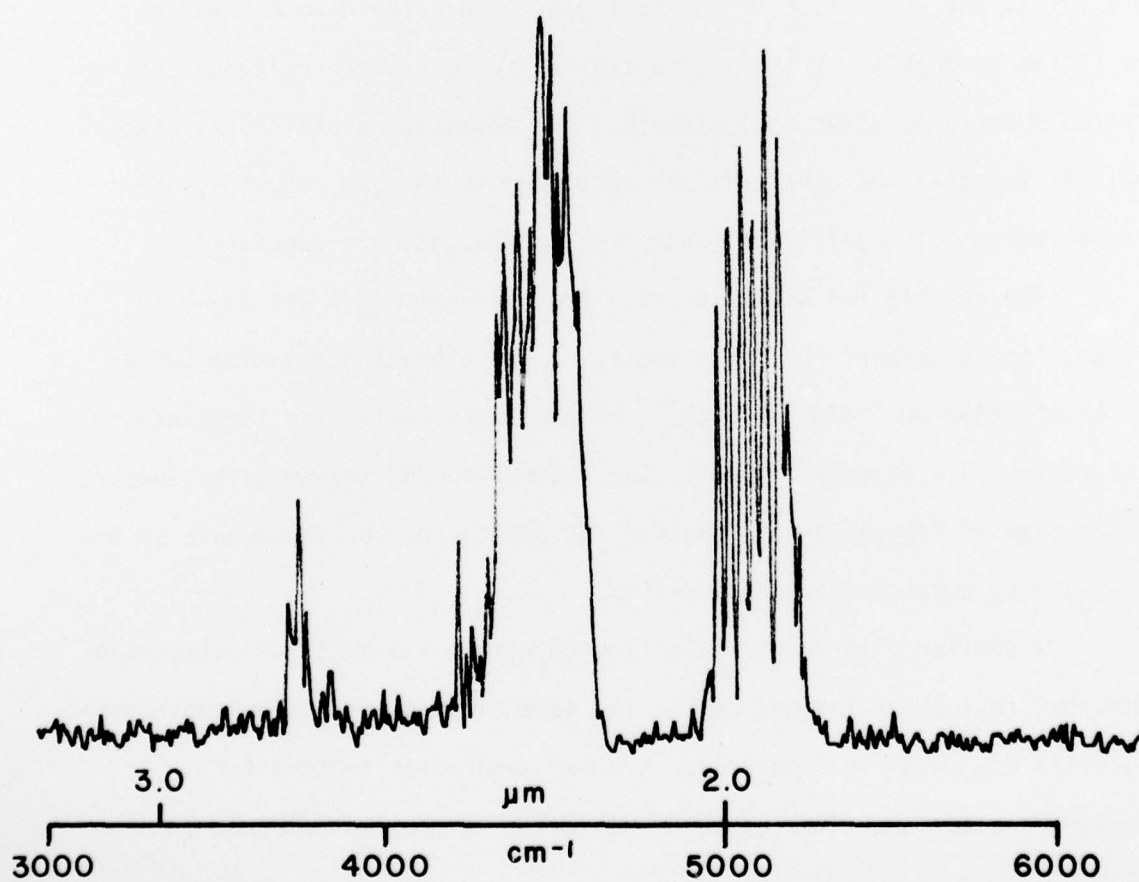


FIGURE 27: Double-beam absorption spectrum of NH_3 vapor in the region of the $(\nu_2 + \nu_3)$ and $(\nu_3 + \nu_4)$ absorption bands.

DOUBLE BEAM INTERFEROMETER

AMMONIA (NH_3)

S.T.P.

L - 100 MM

$\delta\sigma$ - 10 cm^{-1}

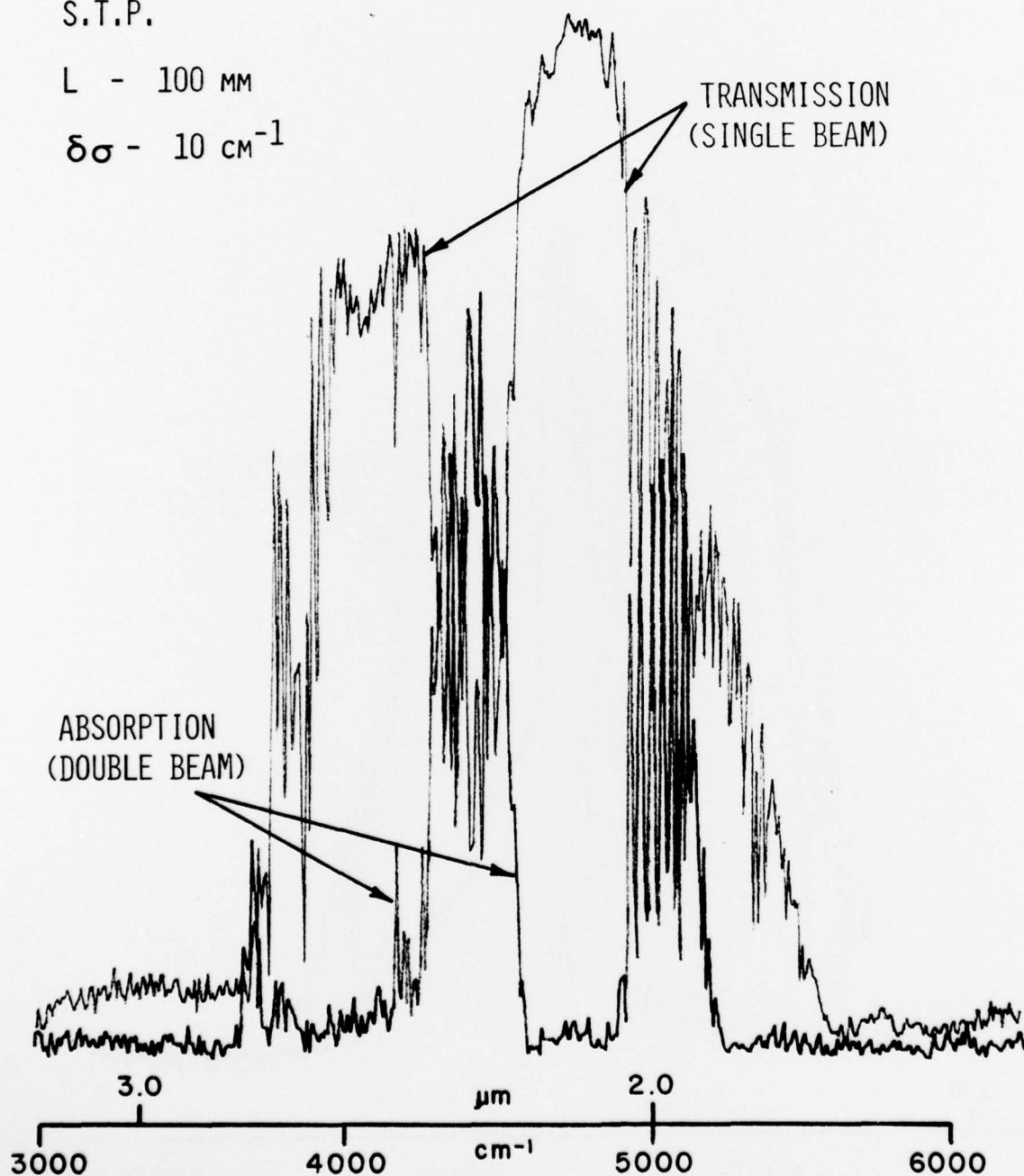


FIGURE 28: Double-beam and single-beam spectra of NH_3 vapor, superimposed for comparison.

DOUBLE BEAM INTERFEROMETER

POLYCARBONATE

1.5 MM THICK

$\delta\sigma - 10 \text{ cm}^{-1}$

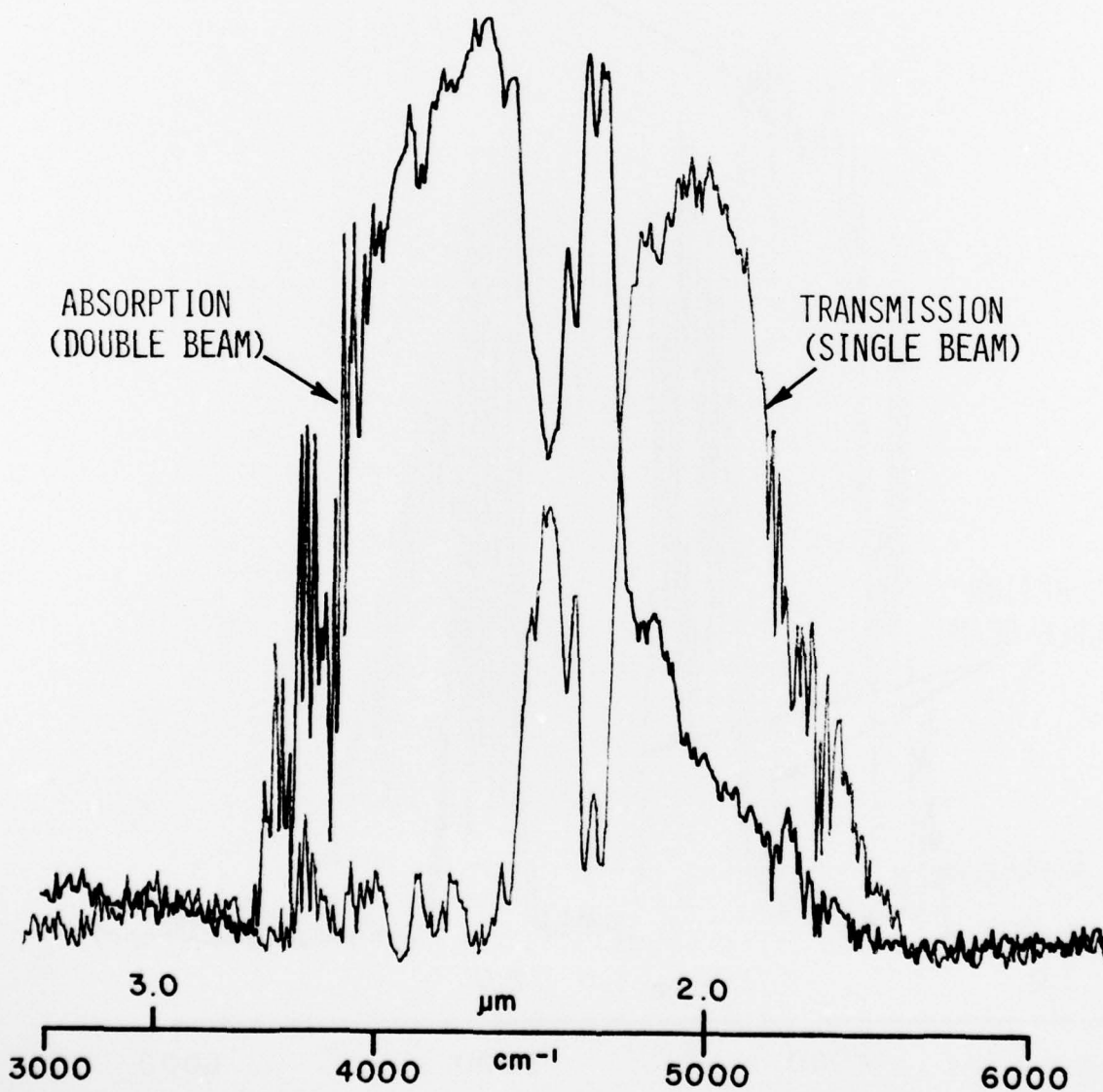


FIGURE 29: Double-beam and single-beam spectra of a 1.5 mm thick polycarbonate filter.

Another experiment, with NH_3 in one of the gas cells, was performed with a spectral resolution of 1 cm^{-1} . The absorption spectrum, taken in the double-beam mode, of the $(\nu_2 + \nu_3)$ band centered near 4450 cm^{-1} is shown in Figure 30. Fine rotation structure, down to 1 cm^{-1} , within the band is clearly evident. An NH_3 absorption spectrum (double-beam) near the same 4450 cm^{-1} band is superposed on the complementary transmission spectrum (single-beam) in Figure 31. The one-to-one correspondence of the fine spectral detail again demonstrates the reality of these features.

The ability of the instrument to suppress spectral structure in the background (away from the absorption features of the test gas; e.g. 15) is demonstrated in Figure 32. The upper trace is the single-beam transmission spectrum of NH_3 in the vicinity of the $(\nu_3 + \nu_4)$ band. Also, clearly present is the $(\nu_2 + \nu_3)$ water vapor feature (ref. 14) centered near 5330 cm^{-1} . The lower trace is the absorption spectrum of NH_3 (double-beam mode). Note the nearly exact correspondence, in both traces, of the NH_3 features, while the water vapor features above 5200 cm^{-1} are completely absent in the double-beam spectrum. The ambient water vapor is common to both beams and is thereby eliminated. In remote sensing applications, this is a powerful tool for removing the spectral contributions from any background sources that lie along the line-of-sight to the object being studied.

Finally, for completeness, we show the 1 cm^{-1} resolution transmission spectra for laboratory air containing water vapor in the ν_1 and ν_3 bands centered near 3700 cm^{-1} (Figure 33) and the $(\nu_2 + \nu_3)$ band centered at 5330 cm^{-1} (Figure 34).

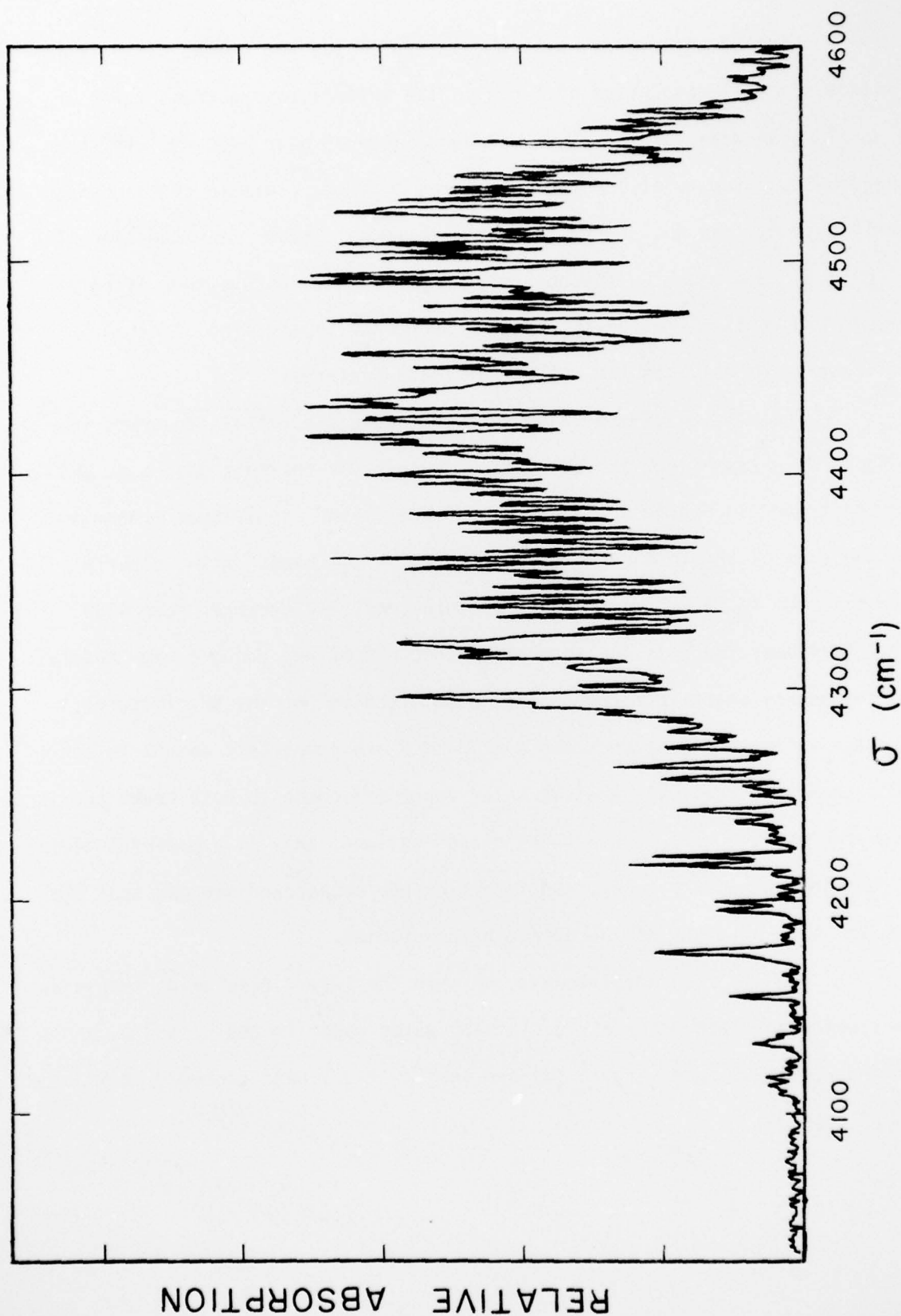


FIGURE 30: Double-beam absorption spectrum of NH₃ vapor near the ($\nu_2 + \nu_3$) band. The spectral resolution is 1 cm⁻¹.

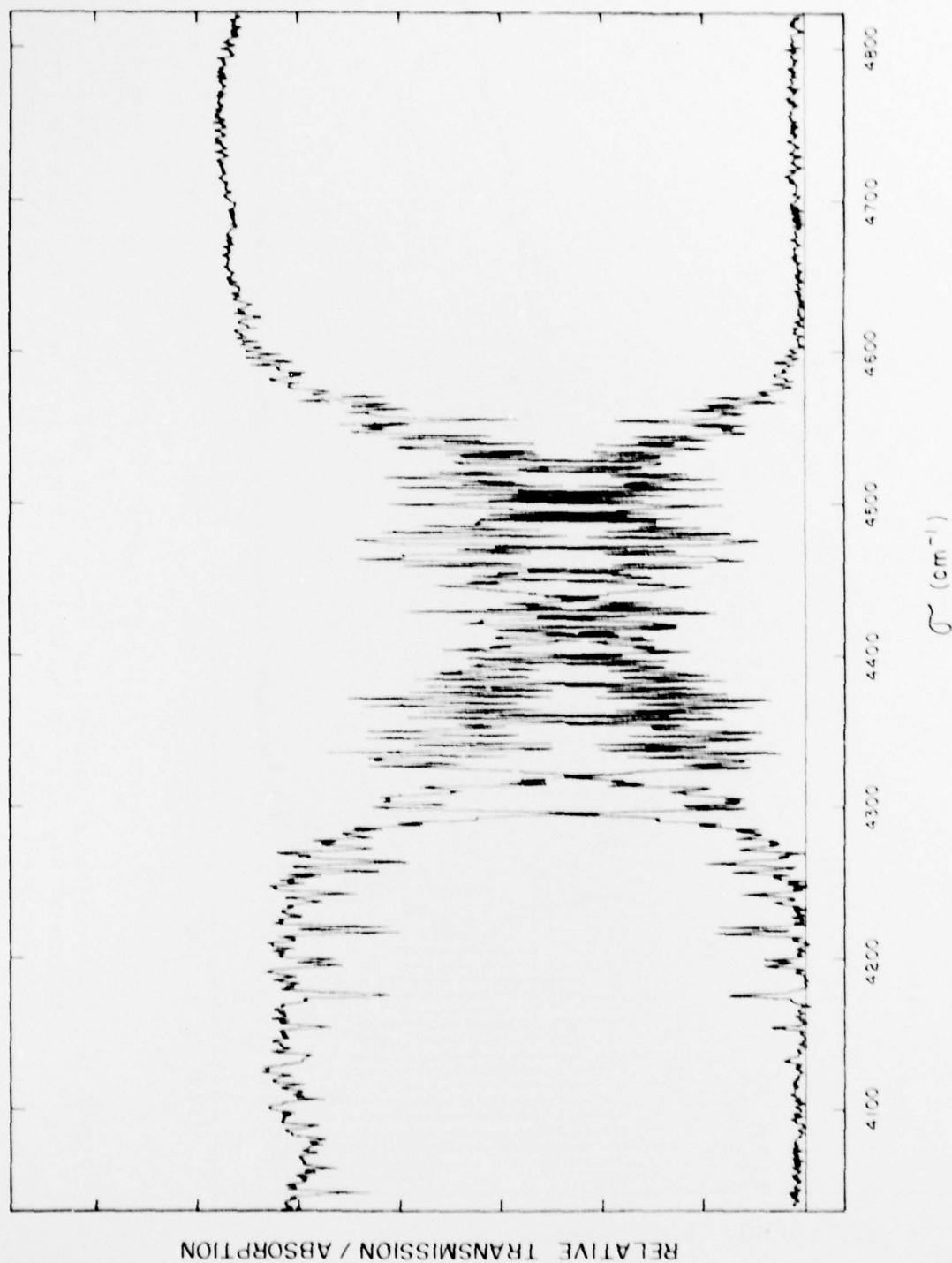


FIGURE 31: Superposition of double-beam (lower trace) and single-beam (upper trace) spectra of NH_3 vapor near the $(\nu_2 + \nu_3)$ band (1 cm^{-1} resolution).

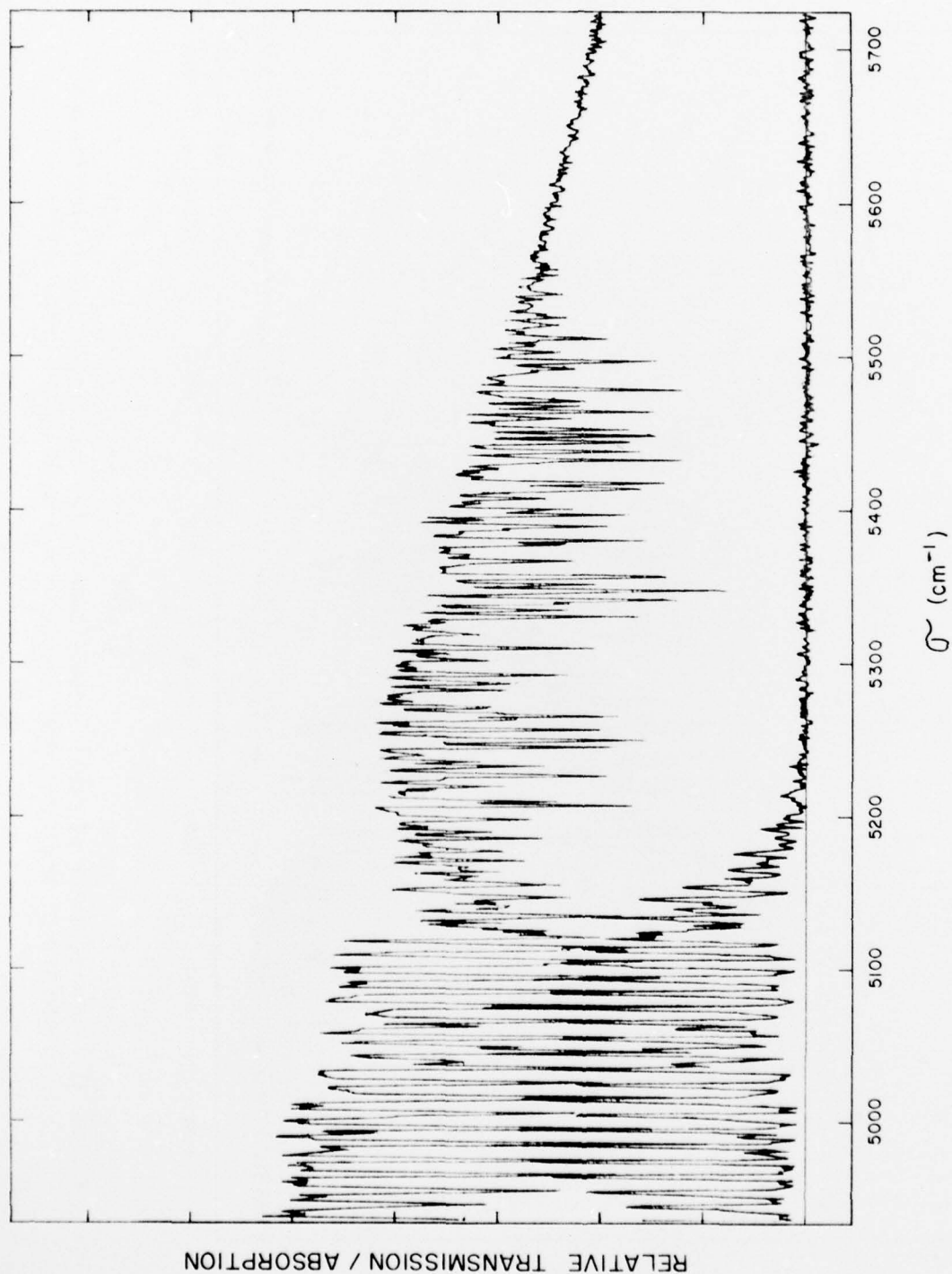


FIGURE 32: Superposition of double-beam (lower trace) and single-beam (upper trace) spectra of NH_3 vapor in the vicinity of the ($\nu_3 + \nu_4$) band. Note the unsuppressed spectrum of H_2O vapor ($>5200 \text{ cm}^{-1}$) in the single-beam spectrum.

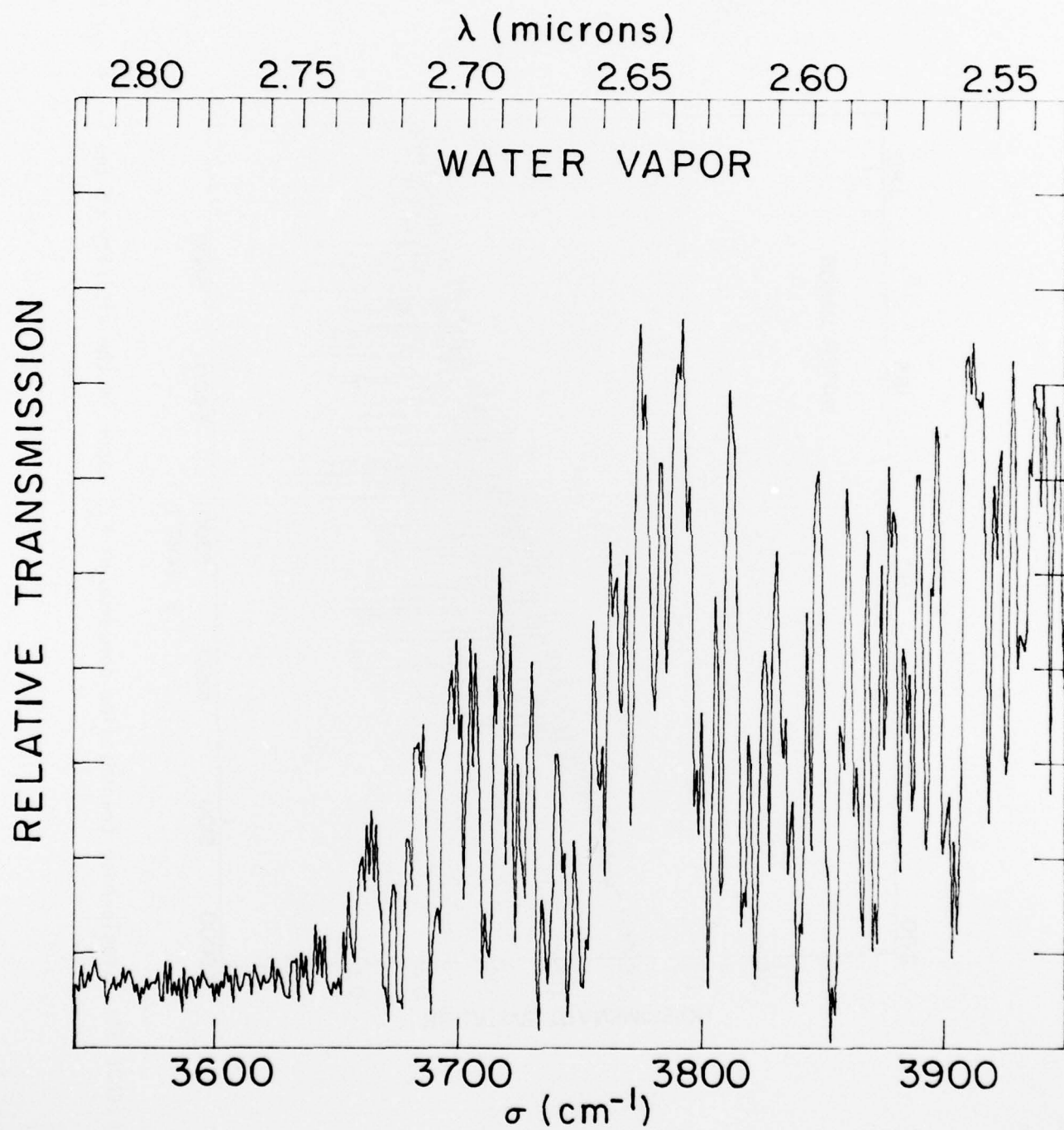


FIGURE 33: Single beam transmission spectrum of the H_2O vapor in the vicinity of the ν_1 and ν_3 bands (1 cm^{-1} resolution).

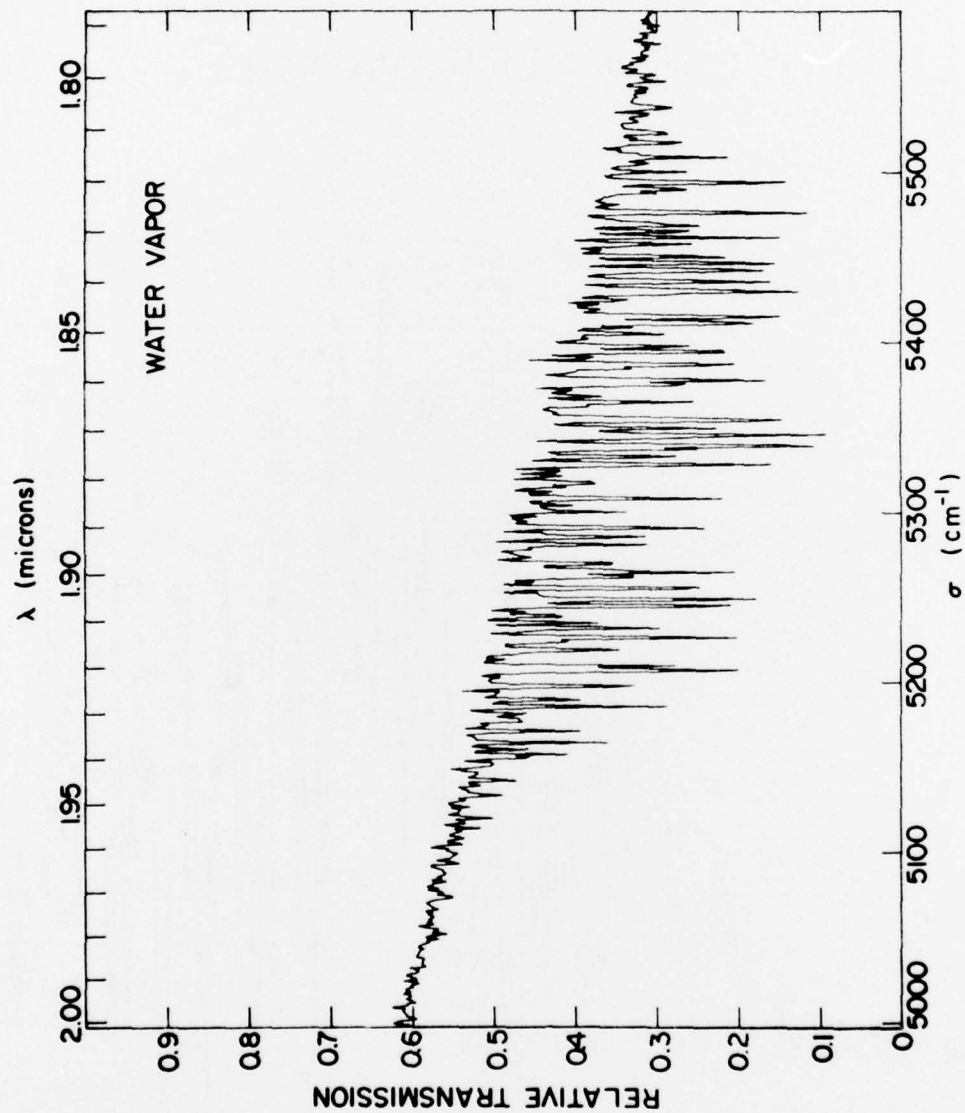


FIGURE 34: Single-beam transmission spectrum of H₂O vapor in the vicinity of the ($\nu_2 + \nu_3$) band.

5. CHARACTERISTICS AND APPLICATIONS OF DOUBLE-BEAM INTERFEROMETRY

In this report we have demonstrated both empirically and computationally that the double-beam interferometer-spectrometer is a highly efficient tool for the remote sensing of localized sources in the presence of strong spatially structured background in the IR region of the spectrum (§ 2 and 4). The Visidyne double-beam interferometer with tailored modulation transfer functions (§ 2) utilizes both spatial and spectral filtering (§ 4) to achieve enhanced sensitivity to localized sources. In the double-beam mode, the interferometer suppresses radiation that is common to both beams, regardless of its spectrum. This includes diffuse background radiation in the vicinity of the source of interest, absorbing or emitting contaminants along the line of sight to the source, and background (other than detector noise) originating from within the interferometer. Suppression ratios of 100/1 have been achieved with our laboratory interferometer, and there is no obvious reason why this cannot be readily improved to 1000/1 by future modifications. We have also shown that background structure with higher spatial frequency components, that is not eliminated by spatial filtering, can be suppressed if its spectral composition is distinguishable from that of the source of interest.

The background suppression capabilities of the Visidyne double-beam interferometer with a tailored MTF have at least two potentially important applications:

- The remote sensing of effluents, e.g., pollution monitoring.
- Surveillance and tracking systems, e.g., the detection of jet plumes or missile trails.

The dual beam system is an imaging system that can be used with a multi-element focal plane detector and it is a diffraction limited system which

preserves spatial, spectral and temporal information. Two characteristics of the double-beam interferometer with tailored MTF that make it superior to conventional detection systems include:

- Selectable Spatial-Frequency Filter
 - i) the system spatial-frequency bandpass can be tailored to respond to target characteristics while suppressing higher and lower spatial frequencies.
- Real Time Optical Background Suppression
 - i) reduces dynamic range and electronic complexity required for processing of weak target signals,
 - ii) reduces the effects of temporal variations in the source or the detectors, and
 - iii) facilitates the extraction of a target signal from background in the case of non-uniform retroreflecting mirror drive
 - iv) suppresses the contribution of channel spectra to the measured interferogram.

The double-beam interferometer is particularly well suited to the remote sensing of stack effluents. For any given observation distance, the MTF of the interferometer can be tailored to respond to the volume of space immediately surrounding the smokestack while suppressing background radiation that corresponds to significantly larger or smaller angular sizes. In practice, regions of concentrated pollutants with linear sizes from a fraction of a meter to tens of meters could be observed with our laboratory interferometer at any distance from ~ 100 m to tens of kilometers by varying the fore optics

(e.g., the telescope) and the defocusing lens. A mosaic focal plane detector is not required for this application.

The double-beam interferometer is equally well suited for use in surveillance. The spatial filter can be tailored to the size of the plume if the target is measured in emission or to the size of the aircraft or missile if the target is measured in obscuration.

REFERENCES

1. Fellgett, P., Colloques Internationaux Du Centre National de la Recherche Scientifique, Les Progres Récents en Spectroscopie Interferentielle, Bellevue, 53 (1957).
2. Connes, J. and Connes, P., J. Opt. Soc. Am., 56, 901 (1966).
3. Vanasse, G.A., Murphy, R.E. and Cook, F.H., Applied Optics, 15, 290 (1976).
4. Beer, R., Norton, R.H. and Seaman, C.H., Rev. Sci. Inst., 42, 1393 (1971).
5. Hall, D., J. Opt. Soc. Am., 66, 1081 (1976).
6. Chandrasekhar, H.R., Genzel, L. and Kuhl, J., Opt. Comm., 17, 106 (1976).
7. Genzel, L. and Kuhl, J., Infrared Physics, 18, 113 (1978).
8. Vanasse, G.A., Stair, A.T., Shepherd, O. and Reidy, W.P., "Background Optical Suppression Scheme (BOSS)", AFGL-TR-77-0135 (June 1977).
9. Dainty, J.C. and Shaw, R., Image Science (Academic Press, London), p. 124 (1974).
10. Fried, D.L. and Williams, R.D., "Formalism Development and Sample Evaluation of the Mean-Square Background Clutter Leakage for a HALO-Type Signal Processor", the Optical Sciences Company, Report Number TR-239 (1977).
11. Kulgein, N.G., Background Measurements Program, Second Special Technical Report, Flight Measurements, LMSC D506988 Lockheed Missile and Space Co., Inc., Palo Alto, California (September 1976).
12. Mertz, L., Transformations in Optics (John Wiley & Sons, Inc., New York 1965).
13. Doty, J., Ph.D. Thesis, Massachusetts Institute of Technology (1979).
14. Herzberg, G., Molecular Spectra and Molecular Structure II (D. van Nostrand, London 1945).